

X-ICP: Localizability-Aware LiDAR Registration for Robust Localization in Extreme Environments

Turcan Tuna^{†,‡}, Julian Nubert[†], Yoshua Nava[‡], Shehryar Khattak[†], Marco Hutter[†]

Abstract—Modern robotic systems are required to operate in challenging environments, which demand reliable localization under challenging conditions. LiDAR-based localization methods, such as the Iterative Closest Point (ICP) algorithm, can suffer in geometrically uninformative environments that are known to deteriorate registration performance and push optimization toward divergence along weakly constrained directions. To overcome this issue, this work proposes i) a robust multi-category (non-)localizability detection module, and ii) a localizability-aware constrained ICP optimization module and couples both in a unified manner. The proposed localizability detection is achieved by utilizing the correspondences between the scan and the map to analyze the alignment strength against the principal directions of the optimization as part of its multi-category LiDAR localizability analysis. In the second part, this localizability analysis is then tightly integrated into the scan-to-map point cloud registration to generate drift-free pose updates along well-constrained directions. The proposed method is thoroughly evaluated and compared to state-of-the-art methods in simulation and during real-world experiments¹, underlying the gain in performance and reliability in LiDAR-challenging scenarios. In all experiments, the proposed framework demonstrates accurate and generalizable localizability detection and robust pose estimation without environment-specific parameter tuning.

Index Terms—robust localization, LiDAR localizability, constrained ICP, optimization degeneracy, environment degeneracy

I. INTRODUCTION

RELIABLE robot pose estimation and map creation are core capabilities that enable mobile robots to operate autonomously. While it is possible to achieve robot localization with global positioning or fixed physical references (e.g., markers), these methods are expensive or difficult to scale to new environments. With the advent of increasingly capable exteroceptive sensors, the research community has focused on solving the *simultaneous localization and mapping* (SLAM) problem with a variety of algorithms [1], [2]. While SLAM can be achieved with different types of sensors [3], this work focuses on LiDAR-based sensing due to its ability to provide reliable and accurate range measurements in the form of point clouds. The success of LiDAR-based approaches in competitions such as the KITTI [4] or the recent HILTI [5] benchmarks, support the strength of LiDAR-based approaches.

This work is supported in part by the EU Horizon 2020 programme grant agreement No.852044, 101016970 and 101070405, EU Horizon 2021 programme grant agreement No 101070596, the NCCR digital fabrication and robotics, the ETH Zurich Research Grant, the SNSF project No.188596, and the Max Planck ETH Center for Learning Systems.

[†]The authors are with the Robotics Systems Lab, ETH Zürich.

[‡]The authors are with the ANYbotics A.G.

¹<https://youtu.be/f-i-br-I5QA>

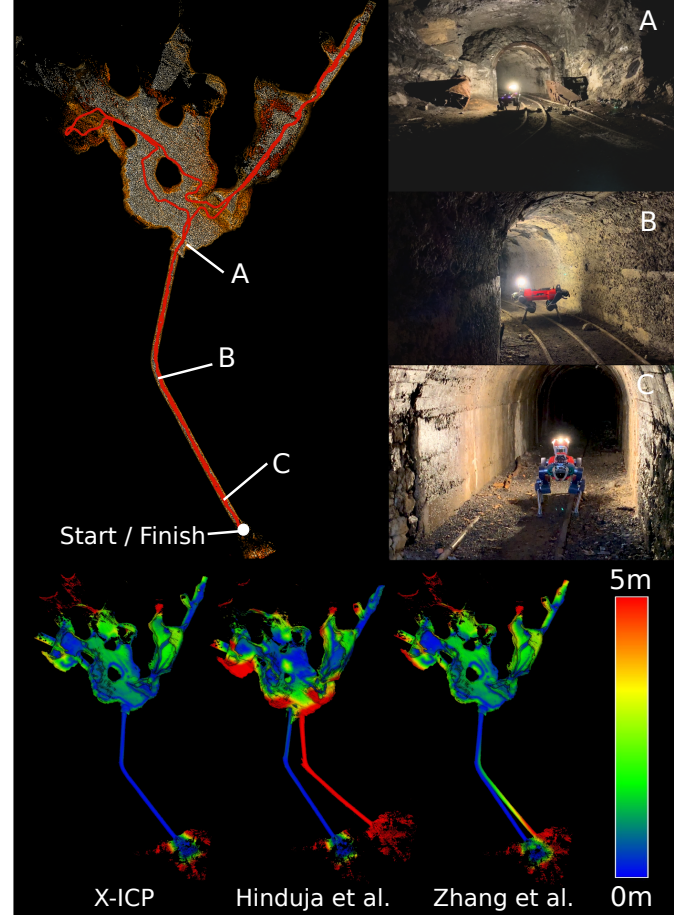


Fig. 1. **Top Row:** Ground truth map and path of the Seemühle experiment (VLP-16). Certain sections of the environment are illustrated through real images. **Bottom Row:** Point cloud maps of the proposed approach in comparison to two other state-of-the-art methods.

a) Point Cloud Registration: Most popular LiDAR-SLAM algorithms perform point cloud registration using iterative minimization techniques to estimate the pose difference between two point cloud scans correctly, often referred to as *scan-to-scan* registration. Similarly, the registration can be done globally against a topological map referred to as *scan-to-map*, which can significantly reduce drift compared to its local counterpart. In a typical LiDAR-SLAM framework, scan-to-map registration is the core step where new data is added to the map. The most prominent point cloud registration method is the *iterative closest point* (ICP) algorithm [6], [7]. Feature- or surfel-based variants of ICP registration, such as LOAM [8] or SUMA [9], are prominent choices in field robotic applications due to their real-time capabilities, as

demonstrated by their use in the DARPA SubT challenge [10]. However, recent research [11], [12] and better computing capabilities allow the usage of point-wise registration, which is free of hand-crafted feature selection and can lead to accurate results over a large set of environments.

b) *Limitations*: Although the ICP algorithm and its variants are arguably among the preferred registration methods to date, its usage requires the consideration of its limitations in practical applications. Four different sources of error are found to be affecting the ICP algorithm [13], [14]. These include the risk of converging to local minima, the sensitivity to sensor bias and noise, an inaccurate initial transformation, and the lack of geometric constraints in the underlying optimization problem. While the robotic community developed methods and systems that attenuate the first three sources, the latter can still drive modern robotic systems to failure when deployed in difficult environments. In (near) self-symmetrical environments, the geometric constraints along the axis of symmetry are (almost) indistinguishable from noise. As a result, the optimization might converge to a noise-induced optimum [15], referred to as a *degraded* or *degenerate* situation. Tunnels, open spaces, corridors, and doorways can be instances of such degraded environments [16], cf. the top row of Fig. 1 for a real-world underground tunnel example.

c) *Localizability-Awareness*: To enable robots to operate in *all* scenarios, including degenerate planar or tunnel-like environments, so-called localizability-awareness is required [17]–[19]. The coping mechanism is two-fold: i) first, the detection of the degeneracy, and ii) second, the mitigation of its negative effects on the optimization. Multiple methods utilize information theory to detect the degradation of the optimization as binary - degraded or not - without considering individual axes of motion [20]–[23]. However, despite being practical and simple, such analysis does not provide adequate detail about the degradation of the optimization in different directions. As a result, most of the solutions [18]–[20] prefer to discard the registration result for the entire measurement rather than salvaging the problem at least along the well-informed directions. Furthermore, as shown in [17], existing detection approaches such as [15], [24] can perform well in practice but require tedious parameter tuning for different environments or sensor configurations.

d) *Proposed Solution*: As a response to the aforementioned challenges, this work proposes a robust localizability-aware point cloud registration framework, **X-ICP**, that enables LiDAR-based SLAM systems to operate in featureless *eXtreme* environments. The proposed framework, shown in Fig. 2, solves both the detection and mitigation of degeneracy. The two sub-modules are *localizability detection* module, abbreviated as *Loc.-Module*, and *optimization* module, abbreviated as *Opt.-Module*. The **Loc.-Module** utilizes the point and surface-normal correspondences between the scan and the map to analyze the alignment strength along the optimization's principal directions. In contrast to prior work [17], this localizability detection applies to the scan-to-map registration and is independent of the robot orientation with respect to the environment. Allowing for reliable detection in various environmental configurations, such as underground scenarios

and large outdoor environments, without online parameter modifications. The resulting estimation is fine-grained, i.e., classifies the current robot state into either $\{\textit{localizable}, \textit{partially-localizable}, \textit{and non-localizable}\}$ categories.

On the other hand, the **Opt.-Module** utilizes the localizability information to calculate and integrate optimization constraints into the low-level optimization of the point cloud registration. Notably, the Opt.-Module is independent of the ICP cost function and can be used independently in combination with other optimization-based systems. The adverse effects of the degenerate directions are mitigated through their direct consideration within the iterative optimization procedure. The result of this optimization utilizes the information contained in the sensing while using external information along the ill-conditioned directions.

The proposed framework is tested extensively on multiple real-world missions in varying environmental and sensory conditions. The real-world experiments and analyses suggest that the proposed framework can reliably detect localizability in various environmental conditions without situation-specific parameter tuning and achieves high robustness and accuracy in degraded environments. The proposed framework consistently outperforms the state-of-the-art robotic approaches [15], [24] throughout all experiments performed in challenging and partly degenerate scenarios, cf. Fig. 1 for an example in a tunnel-like environment.

e) *Contributions*: The main contributions are as follows:

- The development and integration of a multi-level and robust localizability detection algorithm for scan-to-map registration. A detailed ablation study is carried out to investigate the effect of multi-level detection.
- A novel localizability-aware constrained ICP optimization module is developed and tightly coupled with the localizability detection to mitigate the effects of degeneracy.
- A variety of experiments is conducted to evaluate the efficacy of the proposed framework and to compare the results against the state-of-the-art methods. Furthermore, additional content, data, and supplementary material are provided².

II. RELATED WORK

LiDAR-based SLAM systems, at their core, rely on point cloud registration methods to estimate the robot pose. A brief review of these methods is presented in Section II-A. Furthermore, related work to degeneracy detection is discussed in Section II-B, followed by a discussion of the scholarly works that constrain the underlying ill-conditioned optimization problem for point cloud registration in Section II-C.

A. Point Cloud Registration Methods

Point cloud registration is considered a mature research field, and multiple unique approaches [8], [9], [25], [26] are proposed to achieve robust, fast, and accurate pose estimation.

²See the project website for additional results, data, and videos: <https://sites.google.com/leggedrobotics.com/x-icp>

Among these, the most widely used registration algorithm for LiDAR-based registration is arguably the ICP algorithm [27]. The ICP algorithm iteratively finds the transformation between two point clouds given an initial transformation. This is achieved by minimizing a pre-defined cost function that measures the error between point pairs in source and target clouds. Various cost functions have been proposed, such as the point-to-point [6], point-to-plane [7], point-to-line [28], point-to-Gaussian [29], and symmetric point-to-plane [30]. Beyond that, works also combine different cost functions, statistical measures [26], [31], and even employ data-driven methods [16] to achieve more robust registration. Despite these promising alternatives, the point-to-plane cost function [7] is still among the preferred solutions for state-of-the-art robust LiDAR-SLAM systems [32]–[34] for its simplicity and effectiveness, as demonstrated in challenging real-world deployments [3], [5].

B. Degeneracy Detection

Point cloud registration techniques have demonstrated exemplary performance in various practical applications; however, the underlying optimization problem can degenerate in challenging geometrically symmetric environments. This problem is often noticed in the form of *LiDAR-slip* when traversing along self-similar directions of the environment, severely degrading the robot pose estimation performance. Many techniques have been proposed to detect such degeneracy conditions by modeling it as part of the uncertainty or covariance of the pose estimation process [13], [14], [35], [36]. However, a unified uncertainty representation is often not tractable regarding sources of individual error and tends to be over-optimistic in [37]. Motivated by this reasoning, direct degeneracy detection methods have been proposed.

1) *Geometric Methods*: Geometric approaches utilize the relation between the registration cost function and the environment to analyze the quality of pose estimation. Among the first to investigate the geometric stability of the point-to-plane ICP, [38] proposed a sampling-based method to select the most valuable points in a scan to improve the conditioning of the optimization process. Building on this idea, Kwok and Tang [39] proposed improvements such as the iterative center of mass calculation, rotation normalization, and cyclic point addition to improve the efficiency of the method. In a similar direction, IMLS-SLAM [40] includes the contribution of a point to the matching procedure to ensure the observability of the optimization; however, the additional overhead makes the method unsuitable for real-time applications. Similarly, a contribution formulation based on the measurements of the environment was proposed by Zhen et al. [19] to estimate localizability in the eigenspace of the Hessian. The corresponding authors measured the constraint strength of a point and surface-normal pair as the sensitivity of measurements w.r.t to the optimization states. Although this formulation is theoretically grounded and well-structured, the given parameterization does not use the full parametric range of the localizability analysis to distinguish the localizable and non-localizable directions. Furthermore, it does not account

for the scale difference between rotation and translation subspaces, and the requires a prior point cloud map of the environment.

The proposed localizability-awareness framework in this work also uses a geometry-based approach, similar to [19], but does not require a prior map of the environment, the scale difference between rotation and translation is taken into account, and the localizability detection is more fine-grained (three levels vs. binary).

2) *Optimization-based Methods*: For degeneracy detection, several approaches have proposed different metrics to quantify the state of the optimization in a binary manner. Such approaches utilize the intrinsic properties of the optimization problem to produce a metric, which can be used as a measure of optimization degeneracy when subject to a threshold. The work in [41] proposes to use the observability Gramian as a measure of insufficient sensor measurements required to constrain the optimization. Similarly, [22], [34], [42] proposed to use the condition number of the optimization Hessian as a single metric for all 6-DoF of the pose estimation problem. With similar reasoning [23], [43] propose to utilize the determinant of the fisher information matrix as the degeneracy detection metric instead. Reasoning that a combined metric for translation and rotational dimensions may be insufficient, [44] proposes to utilize relative condition number to detect optimization degeneracy along each translational direction. In contrast, CompSLAM [33] uses the D-optimality criterion [45] as a degeneracy detection metric to detect under-constrained environments for different modalities of a robust sensor fusion. Although practical in nature, these approaches subject different metrics to a threshold for degeneracy detection, which is not only heuristic in nature but difficult to generalize as these metrics depend on the environment's structure and the amount of information observed during an operation instance. Furthermore, the smooth transition of the optimization problem from degenerate to non-degenerate is difficult to capture with a binary detection method.

For degeneracy-aware LiDAR-SLAM systems, the seminal work of [15] proposes both a degeneracy detection metric *degeneracy factor* and a degeneracy mitigation method *solution remapping*. The *degeneracy factor* utilizes the minimum eigenvalue of the Hessian matrix of the optimization to detect the degeneracy, and the *solution remapping* uses the detected degeneracy to project the optimization solution only along the well-constrained directions. This work has been adopted by multiple LiDAR-SLAM frameworks [33], [46]–[49] and is considered state-of-the-art; however certain aspects can limit its efficacy. *i)* Being binary in nature, the method depends on the heuristic tuning of thresholds for operation in different environments [17]. *ii)* As eigenvalues represent the scale of their respective eigenvectors, thresholds for translation and rotation cannot be represented by a singular value. *iii)* As *solution remapping* projects the solution to the well-constrained directions, it assumes that well-conditioned directions remain completely unaffected by the ill-conditioning. However, this assumption may be incorrect in heavily degenerate environments. Echoing similar reasoning, [24] proposes to improve *solution remapping* by using the relative condition number

of the optimization directions to set the eigenvalue threshold automatically. These [15], [24] state-of-the-art methods are widely adopted in the robotics domain and are used as baseline methods for comparison in this work.

3) *Data-driven Methods*: With the advent of learning-based methods, data-driven methods provide promising alternatives to perform degeneracy detection. The work of [20] formulates localizability as a function of overlap between scans and uses a support vector classifier to learn a risk metric for point cloud registration. In contrast, [35] proposes directly quantifying localizability using a learned pose estimation uncertainty metric. Furthermore, combining covariance estimation and localizability detection, [50] proposes a deep-learned entropy-based metric. Although successful, these methods rely on extensive ground truth data for learning and are unsuitable for real-time operation. To alleviate reliance on data, [17] proposes to leverage simulation for training and only consider the current LiDAR scan to predict a 6-DoF localizability metric. The authors use sparse 3D convolutions to show generalization across different sensors and environments through real-world experiments. However, this approach is limited to scan-to-scan point cloud registration.

C. Constrained Optimization in Point Cloud Mapping

Constrained optimization techniques are well-known in literature; however, their application to point cloud registration is only recently attracted more attention. Among the first, [51] presented a constrained optimization method for penetration-free point cloud registration, improving the quality of pose estimation. Similarly, [52] use non-linear equality constraints to reduce the linearization error of rotation estimation for point cloud registration. To improve robustness against sensor noise and correspondence outliers, [53] proposes to use an augmented Lagrangian to solve a constrained optimization problem by adding each measurement as a separate constraint. A recent work [54] introduces the addition of soft constraints as costs to the ICP optimization to ensure trajectory continuity between different scans. In contrast, [55] formulates the point cloud registration problem as a constrained quadratic program to provide globally optimal point cloud registration results. These methods demonstrate improved robustness and accuracy for the global point cloud registration problem; however, they do not address the utility of constraints towards limiting the effect of degeneracy in the optimization. To address this challenge, and most related to the proposed method, [44] proposes to use the relative condition number to detect degeneracy and to penalize the motion change along the degenerate direction by introducing constraints in a factor graph formulation.

To the best of the authors' knowledge, the only work in this direction is [44]. However, this work is limited to 2D navigation and does not consider the usage of these constraints in low-level ICP optimization. Given the discussion, the use of degeneracy analysis to constrain the ICP registration problem for robot operation in challenging and degenerate environments remains an open problem, that this work aims to address.

III. PROBLEM FORMULATION & PRELIMINARIES

Motivated by the previous findings, this work presents a solution to robot pose estimation and reliable point cloud registration in geometrically challenging and degenerate environments. As the sensory inputs, only LiDAR point clouds and external odometry estimates are utilized, and the proposed solution is split into two parts: localizability detection and constrained point cloud registration. The proposed components can run on a robotic system with limited computational resources in real-time.

A. Problem Formulation

1) *Point Cloud Registration*: The problem of point cloud registration is defined as finding the rigid body transformation $T_{ML} \in SE(3)$, that best aligns a *reading* point cloud of N_p points ${}_L P \in \mathbb{R}^{3 \times N_p}$ in LiDAR frame (denoted as L) to a *reference* point cloud of N_q points, ${}_M Q \in \mathbb{R}^{3 \times N_q}$ in map frame (denoted as M). The rigid transformation $T_{ML} = [R_{ML} | t_{ML}]$, consists of a rotation matrix $R \in SO(3)$, and a translation vector $t \in \mathbb{R}^3$, with $t = [t_x, t_y, t_z]^T$. For each reading point ${}_L p \in \mathbb{R}^3$ in ${}_L P$, the closest reference point ${}_M q \in \mathbb{R}^3$ in ${}_M Q$, is found through a correspondence search, often in the form of a *k-d tree*. This data association process is defined as $\mathcal{M} \in \mathbb{R}^{6 \times N} = \text{matching}({}_L P, {}_M Q, T_{LM, \text{init}}) = \{({}_M p, \{{}_M q, {}_M n\}) : ({}_M p \in {}_M P), ({}_M q \in {}_M Q)\}$ where ${}_M p$ and ${}_M q$ are the matched point pairs and ${}_M n \in \mathbb{R}^3$, $\|{}_M n\| = 1$ is the surface-normal vector of point ${}_M q$. Furthermore, $N \leq N_p$ is the number of matched points and indicates the size of the problem for the rest of the work. The initial transformation $T_{LM, \text{init}}$ is often provided as an initial guess to transform the scan data to the reference frame to improve the matching process and optimization convergence characteristics. While the accuracy of this initial transformation is critical for the convergence of the minimization [14], the effects of the quality of this initial transformation are not in the scope of this work.

There are multiple ways to define an error function for point cloud alignment; in this work, the point-to-plane [7] cost function will be used. The ICP minimization problem with point-to-plane cost function can be defined as follows:

$$\min_{R, t} \sum_{i=1}^N \left\| ((R p_i + t) - q_i) \cdot n_i \right\|_2. \quad (1)$$

Different solvers, such as singular value decomposition (SVD) [56], LU decomposition, Gauss-Newton, and Levenberg-Marquardt, can be used to solve this minimization problem. In this work, the focus lies on direct linear algebra solvers like SVD, which directly operate in matrix form.

Following the derivation of Pomerleau et al. [57], introducing the scalar triple product and rotation matrix linearization, the minimization (1) can be reformulated as a quadratic cost

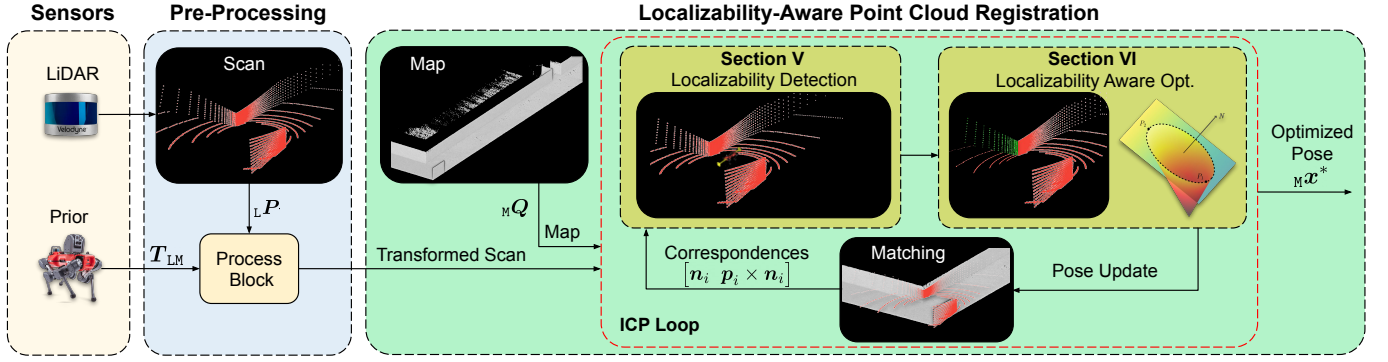


Fig. 2. Overview of the proposed localizability-aware point cloud registration framework. The pose prior is used to transform and undistort the input point cloud, which is together with the existing point cloud map fed to the iterative ICP optimization loop. The optimized drift-free pose within the ICP loop is calculated using the proposed localizability detection (Section V) and aware optimization (Section VI) modules.

optimization problem in the following form:

$$\min_{\mathbf{x} \in \mathbb{R}^6} \mathbf{x}^T \left(\underbrace{\sum_{i=1}^N \begin{bmatrix} (\mathbf{p}_i \times \mathbf{n}_i) \\ \mathbf{n}_i \end{bmatrix}}_{\mathbf{A}} \underbrace{\begin{bmatrix} (\mathbf{p}_i \times \mathbf{n}_i)^T & \mathbf{n}_i^T \end{bmatrix}}_{\mathbf{A}^T} \right)_{\mathbf{A}'} \mathbf{x} - 2\mathbf{x}^T \left(\underbrace{\sum_{i=1}^N \begin{bmatrix} (\mathbf{p}_i \times \mathbf{n}_i) \\ \mathbf{n}_i \end{bmatrix}}_{\mathbf{A}} \underbrace{\mathbf{n}_i^T (\mathbf{q}_i - \mathbf{p}_i)}_{\mathbf{b}'} \right) + \text{Const.}, \quad (2)$$

Here $\mathbf{x} = [\mathbf{r}^T \ \mathbf{t}^T]^T \in \mathbb{R}^6$ are the optimization variables, with $\mathbf{r} \in \mathfrak{so}(3)$ being the rotation vector (lie algebra of $SO(3)$) and $\mathbf{t} \in \mathbb{R}^3$. Moreover, $\mathbf{A}' \in \mathbb{R}^{6 \times 6}$ denotes the Hessian of the optimization problem, and $\mathbf{b}' \in \mathbb{R}^6$ incorporates the constraints between the point clouds. The Hessian constitutes the second-moment matrix of the optimization and defines the local behavior of the Jacobian. Moreover, the Equation (2) is in the form of a well-known quadratic minimization with optimization variables \mathbf{x} , and it can be reformulated as a regular least squares optimization formulation as follows

$$\min_{\mathbf{x} \in \mathbb{R}^6} \|\mathbf{A}'\mathbf{x} - \mathbf{b}'\|_2. \quad (3)$$

Solving this minimization problem is simple for a (semi-)positive definite matrix \mathbf{A}' . The solution of this 6×6 linear equation system will result in the optimal alignment translation vector \mathbf{t} and rotation \mathbf{r} under the performed linearizations. During ICP, due to non-linearities and the resulting iterative nature of the algorithm, these operations described here are repeated until convergence.

2) *Operation in Degenerate Environments*: In practical applications, the above point cloud registration can fail in the presence of environmental degeneracy induced by a lack of geometrically informative structures. The solution \mathbf{T}_{ML} of the previous registration is then under-constrained, which means that one or multiple dimensions of the 6-DoF transformation are (almost) not observable from the found correspondences. Consequently, the main problem this work is trying to address is defined as **finding the best transformation \mathbf{T}_{ML}** in the presence of environmental degeneracy, while **determining the**

hard-to-estimate directions. While this is ignored in most prior work, this work proposes a solution specifically for these situations in order to operate in extreme scenarios.

IV. SYSTEM OVERVIEW

Following the previously introduced requirements - to reliably perform both point cloud registration *and* motion estimation - this work proposes X-ICP, a localizability-aware constrained iterative method. An overview of the proposed system is shown in Fig. 2. The proposed novel components to detect and mitigate the degeneracy, the **Loc.-Module** and the **Opt.-Module**, are embedded into the scan-to-map registration system Pharos [58], [59], developed by ANYbotics. Though, it is worth noticing that the proposed components can be integrated into any iterative optimization-based registration method. Pharos runs at 5 Hz and is tightly coupled with the point-to-plane ICP implementation of the well-known point cloud registration library *libpointmatcher* [59]. Moreover, Pharos utilizes external odometry pose estimates to compensate for the point cloud distortion and as the registration prior $\mathbf{T}_{ML,init}$, enabling scan-to-map correspondence search.

A. Localizability Detection Module Overview

The goal of the **Loc.-Module** is to approximate the null space of the ICP optimization Hessian \mathbf{A}' . A *localizability vector* spanning all 6-DoFs of the optimization problem is introduced to achieve this goal. This localizability vector indicates which eigenvectors are within or should be considered within Hessian's null space. The localizability vector is defined as

$$\mathbf{\Omega} = \{\mathbf{\Omega}_t, \mathbf{\Omega}_r\} \in \mathbb{R}^6 \\ = (\{\mathbf{\Omega}_{L\mathbf{v}_{t1}}, \mathbf{\Omega}_{L\mathbf{v}_{t2}}, \mathbf{\Omega}_{L\mathbf{v}_{t3}}\}, \{\mathbf{\Omega}_{L\mathbf{v}_{r1}}, \mathbf{\Omega}_{L\mathbf{v}_{r2}}, \mathbf{\Omega}_{L\mathbf{v}_{r3}}\})^T, \quad (4)$$

where $\{\mathbf{L}\mathbf{v}_{t1}, \mathbf{L}\mathbf{v}_{t2}, \mathbf{L}\mathbf{v}_{t3}\} \in \mathbf{V}_t$ are the translational eigenvectors of the Hessian \mathbf{A}' corresponding to \mathbf{t} variables and expressed in the LiDAR frame, whereas $\{\mathbf{L}\mathbf{v}_{r1}, \mathbf{L}\mathbf{v}_{r2}, \mathbf{L}\mathbf{v}_{r3}\} \in \mathbf{V}_r$ correspond only to the rotation \mathbf{r} . Importantly, as discussed in Section II-A, the Jacobian of ICP consists of two independent elements, the \mathbf{n} and $\mathbf{p} \times \mathbf{n}$ for translation and rotation, respectively. This is not a design choice of the proposed framework but an inherent property of the point-to-plane cost

function. In order to keep this property valid, in this work, the cross-covariances between translation and rotation components of the Hessian are omitted in the localizability analysis. As a consequence, only the translational and rotational eigenvectors are required.

More details on how to obtain \mathbf{V}_t and \mathbf{V}_r are explained in step V-A of Section V.

The localizability categories Ω represent the localizability state of each eigenvector in the form of a categorical variable; this discrete localizability space is defined as $\Omega_i \in \{none, partial, full\}$, where the categories correspond to being non-localizable, partially-localizable and localizable, respectively. The sequence of actions for each of these categories will be explained in step V-C of Section V.

B. Localizability Aware Optimization Module Overview

Utilizing the output of the Loc.-Module, i.e. the discrete set of localizability categories Ω , the goal of the **Opt.-Module** is defined as constructing and solving the constrained optimization problem that will be used for finding the optimal solution \mathbf{x}^* of the optimization problem (3). This process is explained thoroughly in Section VI. In this part, constrained optimization techniques based on Lagrangian-multipliers are used to obtain the best possible solution given the observed localizability.

The complete system is visualized in Fig. 2, offering reliable robot pose estimation in the presence of LiDAR degeneracy. The main contributions of this work are explained and highlighted in Sections V and VI.

V. LOCALIZABILITY DETECTION MODULE

In this section, the details of the **Loc.-Module** are described according to the information flow shown in Fig. 3. Localizability detection aims to measure the information within the correspondences to identify the under-constrained directions correctly. As shown in Fig. 3, given the correspondences, the first task is the **Information Analysis**, analyzing the relations between the Hessian and the geometric information from the environment. In the second step, **Filtering**, the redundant information from the **Information analysis** step is filtered out. Finally, the filtered information is interpreted, leading to a fine-grained **Categorization**. After the correspondence search, the matched correspondences are transformed back to the LiDAR frame L to eliminate the effect of the map's physical size, and the localizability analysis is performed in this frame.

A. Information Analysis

1) *Eigenanalysis*: The information analysis starts with an eigenanalysis of the Hessian matrix of the optimization problem. For the derivation of the matrix for a point-to-plane ICP cost function, the reader is referred to Section IV, where the Hessian is provided as \mathbf{A}' in Equation (3). The Hessian can be divided into sub-matrices based on the relation of the minimization variables \mathbf{x} :

$$\mathbf{A}' = \begin{bmatrix} \mathbf{A}'_{rr} & \mathbf{A}'_{rt} \\ \mathbf{A}'_{tr} & \mathbf{A}'_{tt} \end{bmatrix}_{6 \times 6}.$$

Here, $\mathbf{A}'_{rr} \in \mathbb{R}^{3 \times 3}$ exclusively contains information related to the rotation variables. Similarly, $\mathbf{A}'_{tt} \in \mathbb{R}^{3 \times 3}$ exclusively contains information related to the translation variables.

It is not trivial to treat $t \in \mathbb{R}^3$ and $r \in \mathfrak{so}(3)$ together. Hence, the analysis is split up into two separate decompositions; the eigenanalysis of \mathbf{A}'_{tt} and \mathbf{A}'_{rr} are performed using SVD. For the rotation and translation components, the eigen-decomposition is given as

$$\mathbf{A}'_{tt} = \mathbf{V}_t \Sigma_t \mathbf{V}_t^\top, \quad \mathbf{A}'_{rr} = \mathbf{V}_r \Sigma_r \mathbf{V}_r^\top,$$

where $\mathbf{V}_t \in SO(3)$ and $\mathbf{V}_r \in SO(3)$ are the eigenvectors in matrix form, and $\Sigma_t \in \{\text{diag}(\mathbf{v}) : \mathbf{v} \in \mathbb{R}_{\geq 0}^n\}$ and $\Sigma_r \in \{\text{diag}(\mathbf{v}) : \mathbf{v} \in \mathbb{R}_{\geq 0}^n\}$ are diagonal matrices with the eigenvalues of \mathbf{A}'_{tt} and \mathbf{A}'_{rr} as the diagonal entries, respectively. Interestingly, the eigenvalues in Σ_t and Σ_r provide a direct measure of the information along each eigenvector it is paired with. However, as discussed in Section II, eigenvalues can behave inconsistently for different environments and sensors, and hence are not used directly in this work's localizability estimation.

2) *Information Pair Contribution*: The second part of the proposed information analysis is to formulate the contribution of each **information pair**, defined as (\mathbf{p}, \mathbf{n}) . A formal relationship is required between the information pairs and the cost to assess how much a pair contributes to the cost. Similar to other works [38], [39], [60], the Jacobian matrix of the optimization is chosen as the contribution indicator. It is intuitive to see that the Jacobian matrix \mathbf{A} defined in Equation (2), by definition, measures the change of the cost for the optimization variable \mathbf{x}_i .

a) *Analogy to Classical Mechanics*: In analogy to classical mechanics, the Jacobian measures the magnitude of the wrench induced locally by each information pair. A wrench system consists of force and torque; in the presented application, it can be thought of as if the pair applies force and torque to the solution \mathbf{x} . In the presented case, the force that will translate the solution is defined as the surface-normal \mathbf{n} and the torque that will rotate the solution is defined as $\boldsymbol{\tau} = \mathbf{p} \times \mathbf{n}$. Although intuitive, the torque formulation does not provide a generalizable parametrization in its plain form. The point \mathbf{p} can be at a different distance, leading to a higher torque of farther points, which prevents the generalizability of this formulation in practical applications.

Kwok and Tang [39] studied the effect of this scale difference in the ICP algorithm of different normalization techniques. The study suggests that *maximum norm*-normalization performs better than *average norm*-normalization, as done in [38], or *moment*-normalization. This is true to reliably solve the ICP problem, where one requires the spatial relations between the points; however, this is not the case for point-wise contribution calculation for localizability estimation. Considering this fact and the requirement that the point norm should not affect the contribution value directly, this work proposes to use moment normalization, which will map the torque values to a unit sphere (shown in Equation (5)).

b) *Information Matrix*: For numeric stability, if $|\boldsymbol{\tau}|$ is close to zero (i.e., the vectors are near-parallel), the information pair is dropped. This could happen when a surface-

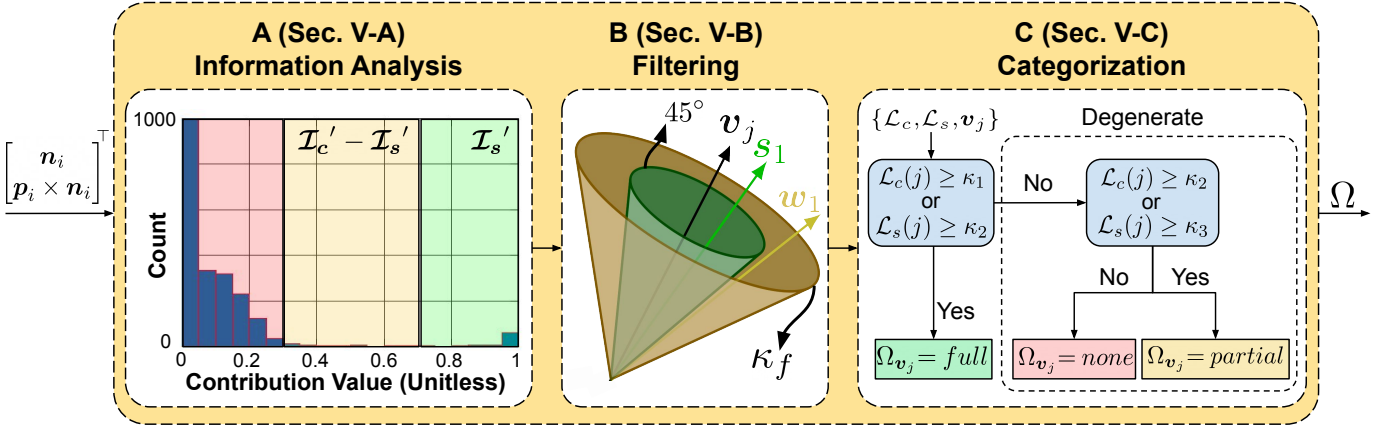


Fig. 3. Overview of the localizability detection module. **A - Information Analysis:** An exemplary histogram shown for one eigenvector \mathbf{v}_j direction. **B - Filtering:** This step investigates the similarity of every alignment vector in the histogram to the eigenvector $\mathbf{v}_j \in \{\mathbf{V}_r, \mathbf{V}_t\}$. Here, \mathbf{s}_1 and \mathbf{w}_1 illustrate strong and weak alignment vectors, respectively. **C - Categorization:** Localizability categories are assigned to each vector based on a decision tree.

normal directly points to the sensor frame. Furthermore, the moment normalization is only applied for information pairs with $|\tau| \geq 1$, preventing mapping of torque values from within the unit sphere, which might push Loc.-Module towards optimistic localizability detections.

After moment normalization of the torque vectors, the wrench systems are stacked for all available information pairs to form the information matrix as follows:

$$\mathcal{F}_r = \begin{bmatrix} \frac{\mathbf{p}_1 \times \mathbf{n}_1}{\|\mathbf{p}_1 \times \mathbf{n}_1\|_2} & \dots & \frac{\mathbf{p}_N \times \mathbf{n}_N}{\|\mathbf{p}_N \times \mathbf{n}_N\|_2} \end{bmatrix}^\top, \quad (5)$$

$$\mathcal{F}_t = [\mathbf{n}_1 \quad \dots \quad \mathbf{n}_N]^\top.$$

Here, $\mathcal{F}_r \in \mathbb{R}^{N \times 3}$ and $\mathcal{F}_t \in \mathbb{R}^{N \times 3}$ are the rotational and translational information matrices, respectively. The final task in the information analysis is then to compute the localizability contribution from \mathcal{F}_r and \mathcal{F}_t .

c) *Localizability Contributions:* The localizability concept is defined in the eigenspace of each eigenvalue, and hence, can be obtained for every eigenvector direction. This ensures that the detection is not affected by the orientation of the LiDAR or the robot w.r.t the environment, which is a crucial advantage in practical applications. Thus, the information matrices defined in Equation (5) are projected onto the eigenspace of the translation and rotation Hessians. To achieve this, the eigenvector matrices \mathbf{V}_r and \mathbf{V}_t will be used as follows:

$$\mathcal{I}_r = (\mathcal{F}_r \cdot \mathbf{V}_r)^{|\cdot|}, \quad \mathcal{I}_t = (\mathcal{F}_t \cdot \mathbf{V}_t)^{|\cdot|}. \quad (6)$$

Here, $\mathcal{I}_r, \mathcal{I}_t \in \mathbb{R}^{N \times 3}$ are the localizability contributions for all information pairs $\{\mathbf{p}, \mathbf{n}\}$, projected by the eigenvectors in $\{\mathbf{V}_r, \mathbf{V}_t\}$. The $(\dots)^{|\cdot|}$ operator indicates the element-wise absolute value of the vector. Concurrently, the scalar values in \mathcal{I}_r and \mathcal{I}_t are direct indicators of localizability contribution of a certain direction. If the scalar value is $\mathcal{I}(i) = 1.0$, the direction's localizability contribution is perfect, and if $\mathcal{I}(i) = 0.0$, the information pair has no contribution to the localizability of this direction.

An example of the localizability contributions can be visualized with a histogram as shown in Fig. 3-A for a single translation eigenvector. The contribution values are dominantly

at the lower-end, indicating low contribution. Nevertheless, there is a high peak at around 1.0, suggesting the presence of a small but highly contributing structure, such as a planar surface with a surface-normal parallel to the eigenvector. While pair-wise quantification of localizability contributions is important, this pair-wise information needs to be filtered and consolidated for categorizing the optimization state.

B. Filtering

Given the localizability contributions defined in Equation (6), $\mathcal{I} = [\mathcal{I}_r, \mathcal{I}_t] \in \mathbb{R}^{N \times 6}$, the goal of the **filtering** step is to remove redundant information and to render the present information interpretable.

1) *Filtering Low Contribution:* An example of redundant information is shown in Fig. 3-A, where the low contribution region highlighted in red dominates the analysis. If the localizability contribution is small, it might become indistinguishable from measurement- or feature extraction noise. This step addresses this issue by employing binary element-wise filtering. The filtering operation is a re-assigning operation defined as follows:

$$\mathcal{I}'_c(i, j) = \begin{cases} \mathcal{I}(i, j), & \text{if } \mathcal{I}(i, j) \geq \kappa_f \\ 0, & \text{otherwise} \end{cases}. \quad (7)$$

Here the indices are defined as $i \in \{1, \dots, N\}$ and $j \in \{1, \dots, 6\}$. \mathcal{I}'_c is the **filtered localizability contribution vector**, which contains all the reliable localizability contribution values. Moreover, κ_f is the filtering parameter, the first user-defined parameter. Since this parameter captures the sensor and feature extraction noise for different LiDAR sensors, it should be re-adjusted. This parameter is set to $\kappa_f = \cos(80^\circ) \approx 0.1736$ throughout all experiments except for Seemühle with Ouster OS0-128, where the different noise-characteristic compared to the Velodyne VLP-16 is considered. The Ouster LiDAR measurements are subject to a higher variance, hence, κ_f is set to $\cos(60^\circ) = 0.5$ to achieve more aggressive filtering.

2) *Filtering High Contribution:* Using this filtered localizability contribution \mathcal{I}'_c , the contributions larger than κ_f , i.e.

the weak and strong ones, can be combined to summarize the available geometrical information:

$$\mathcal{L}_c(j) = \sum_{i=1}^N \mathcal{I}_c'(i, j). \quad (8)$$

Here, $\mathcal{L}_c \in \mathbb{R}^{1 \times 6}$ is the **combined localizability contribution vector** over all reliable information pairs. More correspondences indicate higher available information. At the same time, more correspondences also include more sensor and feature extraction noise. The filtering step of Section V-B1 acts as an outlier rejection step and helps to reduce these effects. Matrix \mathcal{I}_c' still contains weak but reliable contributions, which need to be kept. However, a measure of the strongest contributions is still required to identify the more fine-grained status of the localizability. The filtering step is based on **geometrical vector alignment**; only the alignment values greater than $\cos(45^\circ) \approx 0.707$ will be considered a strong contribution, justified through geometric relations. In Fig. 3-B, the separation of strong and weak alignment regions against an eigenvector is visualized. The inner green cone indicates the region with strong vector alignment, whereas the yellow region indicates the weak. This separation is formulated as follows:

$$\mathcal{I}_s'(i, j) = \begin{cases} \mathcal{I}_c'(i, j), & \text{if } \mathcal{I}_c'(i, j) \geq \cos(45^\circ) \\ 0, & \text{otherwise} \end{cases} \quad (9)$$

$$\mathcal{L}_s(j) = \sum_{i=1}^N \mathcal{I}_s'(i, j),$$

Here, $\mathcal{L}_s \in \mathbb{R}^{1 \times 6}$ is the **strong localizability contribution vector**. Similar to the combined localizability contribution, this expression is also affected by changing N , however, it is less sensitive to the sensor noise and only affected by feature extraction errors. These strong and combined localizability contribution vectors are crucial for the next step, where these vectors will be used to categorize the localizability.

C. Categorization

The final step of the *Loc.-Module* provides the localizability categories given the localizability information from the previous step.

a) Localizability Parameters: To achieve this goal, three localizability parameters are introduced: *i)* Parameter κ_1 is the safety localizability threshold defining the lower bound of being fully localizable. *ii)* Parameter κ_2 regulates the transition from being localizable to partially-localizable and represents the upper bound of being partially localizable. *iii)* Parameter κ_3 is the minimum information threshold that covers the case when the environment has sparse yet well-aligning information and regulates the transition from being partially-localizable to non-localizable.

b) Parameter Choice: The definitions of these thresholds provide natural bounds among the parameters, $\kappa_1 \geq \kappa_2 > \kappa_3$. These parameters are set based on the basin of convergence of the employed ICP algorithm. The rules of setting the parameters are as follows: since κ_1 sets the boundary between being localizable and {partial-localizability, non-localizable},

it can be set arbitrarily high. The only drawback is the computational cost of the localizability detection. An example value of $\kappa_1 = 500$ indicates that the ICP optimization is allowed to run with a minimum of 500 perfectly aligned pairs. On the other hand, setting κ_2 is a system characteristics choice. Jointly with κ_3 , it defines how the partial-localizability should be approached. It should be set between κ_1 and κ_3 . Finally, κ_3 sets the boundary between partial-localizability and non-localizable status. A value of 50 suggests the constrained ICP optimization is allowed to run in a controlled manner with a minimum of 50 sampled pairs. Using these intuitions, in the rest of this work, the localizability parameters are set as $\kappa_1 = 250$, $\kappa_2 = 180$, and $\kappa_3 = 35$ **for all environments and sensors** in Section VII.

c) Decision Tree: These parameters are used in a decision tree to get the localizability categories as shown in Fig. 3-C. The decision tree takes the filtered localizability contribution vectors and an eigenvector as input. The decision tree operates eigenvector-wise; thus, the required binary comparisons are repeated for all 6 directions. First, the optimization is checked whether it is solvable in the eigenvector direction by comparing κ_1 against \mathcal{L}_c and κ_2 against \mathcal{L}_s . If either of these comparisons suggests that the problem is well-constrained, then the direction is localizable, $\Omega_{v_j} = \text{full}$. Secondly, suppose the first comparisons suggest that the problem is not well-constrained; in this case, κ_2 is compared against \mathcal{L}_c and κ_3 against \mathcal{L}_s to understand whether there is information present to salvage in the optimization problem. If either of these comparisons holds, the localizability category is assigned as partial, $\Omega_{v_j} = \text{partial}$, and non-localizable, $\Omega_{v_j} = \text{none}$, otherwise.

d) Xs-ICP - Simplified X-ICP: Although effective and efficient, the main focus of the full X-ICP is the robustness and accuracy of the estimated robot pose, and not the simplicity of the method. In cases where only limited computational resources are available, the previous categorization can be simplified, resulting in the simplified version of the X-ICP algorithm; Xs-ICP. Xs-ICP is a special case of X-ICP, for which the localizability parameters are selected as $\kappa_1 \geq \kappa_2 = \kappa_3$, and the partial-localizability category is discarded to reduce complexity. Without employing partial localizability, Xs-ICP performs localizability detection similar to the literature in a binary fashion. The decision tree of Xs-ICP also simplifies compared to the one shown in Fig. 3-C. In this version of the decision tree, the only carried out comparisons are, $\mathcal{L}_c \geq \kappa_1$ or $\mathcal{L}_s \geq \kappa_3$. If either of these statements holds, the ICP optimization problem is well-constrained in the direction of the eigenvector or non-localizable otherwise. Finally, this categorization step is performed only in the first iteration of the ICP algorithm to save computational time.

VI. LOCALIZABILITY AWARE OPTIMIZATION MODULE

The **Opt.-Module** consists of constraint calculation and constrained optimization steps as shown in Fig. 4. Given the localizability categories Ω and eigenvectors ${}_L v_j$, the objective of this module is to find the optimal optimization variables x^* , even when the optimization is under-constrained. In the

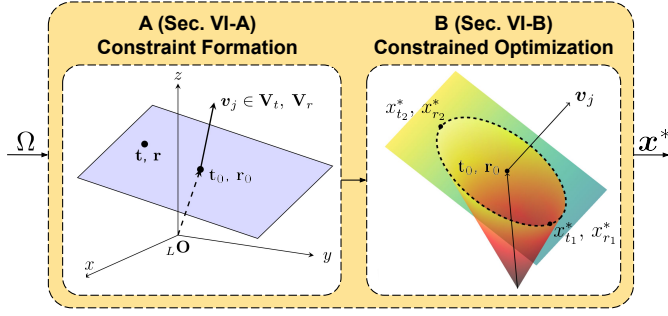


Fig. 4. Overview of the constrained optimization module. The Opt.-Module steps are 1) linear **Constraint Formulation** in the form of a 3D plane, and 2) **Constrained Optimization** employing these constraints.

first step of the *Opt.-Module*, the *Constraint Calculation* (Section VI-A), the actions to take for each localizability category are explained, and the calculation of optimization constraints is laid out in detail. Later, in *Constrained Optimization* (Section VI-B), these constraints will be integrated into the optimization problem. Importantly, since the point cloud registration is done in the map frame M , in this section, all the data is expressed in the map frame. Similarly, the eigenvectors are rotated to the map frame for consistency. At each iteration of ICP, this rotation is calculated as $R_{M,L,0,k} = R_{M,L,0,1} \cdot R_{M,L,1,2} \cdot \dots \cdot R_{M,L,(k-1),k}$, where k refers to the current index of the ICP iteration.

A. Constraint Calculation

First, the form of the constraints is defined as discussed in the information analysis (Section V-A), the eigenvectors of the optimization are in \mathbb{R}^3 , expressed in the same geometrical frames as the optimization variables t and r , allowing for the formulation of a suitable constraint form. Here, the desired direction to be constrained is defined by the eigenvector v_j . Based on whether v_j is of translational or rotational nature, the definition of the constraints changes as follows:

$$\begin{aligned} v_j^\top \cdot (t - t_0) &= 0, & \text{if } v_j \in V_t, \\ v_j^\top \cdot (r - r_0) &= 0, & \text{if } v_j \in V_r. \end{aligned} \quad (10)$$

Here, both lines of Equation (10) define a three-dimensional plane, defined by a normal vector v_j , and a point in the plane t_0 or r_0 for translation and rotation, respectively. An example of a single constraint is illustrated in Fig. 4-A.

1) *Localizability Categories*: Optimization constraints are added based on the localizability category of the corresponding eigenvector v_j . The following three cases are possible:

- If $\Omega_{v_j} = \text{full}$, there is no need to employ any additional constraint.
- On the other hand, if $\Omega_{v_j} = \text{none}$, the corresponding direction is assumed non-localizable, and a full constraint is employed by setting t_0 or r_0 to $0_{3 \times 1}$.
- Finally, if $\Omega_{v_j} = \text{partial}$, the constraint value is calculated by considering the available information from the environment.

The exact procedure for the latter one is explained in the following section.

2) *Partial Localizability*: Calculating the *partial* localizability constraint value requires re-sampling the ICP correspondences from \mathcal{M} . The question of how many pairs need to be re-sampled depends on the process leading to the categorization of being partially-localizable (cf. Fig. 3-C). If the statement $\mathcal{L}_c \geq \kappa_2$ is true, then the information pairs used for calculating \mathcal{L}_c will be re-used for the calculation of the constraint. Otherwise, if the statement $\mathcal{L}_s \geq \kappa_3$ is true, then the information pairs used to calculate the \mathcal{L}_s will be re-used. The re-used information pairs are denoted as $\{^{\text{re}}p, \{^{\text{re}}n, ^{\text{re}}q\}\} \in \mathcal{M}$. For the case of $v_j \in V_t$, the constraint value t_0 can be computed by solving the following minimization problem:

$$\begin{aligned} ^{\text{re}}A_t &= [^{\text{re}}n][^{\text{re}}n]^\top, & ^{\text{re}}b_t &= [^{\text{re}}n]^\top (^{\text{re}}q - ^{\text{re}}p) \\ \min_{t_0 \in \mathbb{R}^3} & \left\| ^{\text{re}}A_t t_0 - ^{\text{re}}b_t \right\|_2. \end{aligned} \quad (11)$$

Similarly, for the case of $v_j \in V_r$ the constraint value r_0 is calculated as follows:

$$\begin{aligned} ^{\text{re}}A_r &= [^{\text{re}}p \times ^{\text{re}}n][^{\text{re}}p \times ^{\text{re}}n]^\top \\ ^{\text{re}}b_r &= [^{\text{re}}p \times ^{\text{re}}n]^\top (^{\text{re}}q - ^{\text{re}}p) \\ \min_{r_0 \in \mathbb{R}^3} & \left\| ^{\text{re}}A_r r_0 - ^{\text{re}}b_r \right\|_2. \end{aligned} \quad (12)$$

The outputs t_0 or r_0 contain the motion estimates based on the re-sampled correspondences in the direction of the degenerate eigenvector v_j . This is possible since in Section V the information analysis confirmed the existence of readily available constraints along the degenerate directions and the re-sampling process selects these noise-free and reliable constraints.

However, as the data used in these minimization problems are deliberately selected to provide information in a specific direction, the Hessian matrices $^{\text{re}}A_t$ and $^{\text{re}}A_r$ might not be well-conditioned in some cases. To mitigate this risk, first, the Hessian matrices are factorized via LU decomposition with pivoting [61]. Here the pivoting operation increases accuracy by interchanging rows to make the pivot element larger than any element below. Later, to reduce the possible adverse effects of ill-conditioning of the factorized problem, RIF preconditioning [62] is applied. Another alternative to this linear algebra approach would be sampling points in the well-constrained directions [38] in addition to the degenerate directions to keep the Hessian conditioning in a good state; however, this is not performed since re-sampling of well-constrained directions adds additional computational burden without a clear gain in performance and robustness.

If these precautions are not taken, under certain conditions the calculated constraint from the re-sampling might not be accurate, and the residual generated through projection onto the eigenvectors might affect the well-constrained directions negatively.

B. Constrained Optimization

In the final step, the calculated constraint values t_0 and r_0 are integrated into the unconstrained least squares minimization problem to obtain the optimal solution x^* . Note that the individually defined translation and rotation constraints

from Equation (10) are required to be applied to the ICP optimization problem. As a result, the constraints must be extended to be applied to a 6-DoF optimization problem. The extended and re-arranged constraints are shown below:

$$\begin{aligned} [0_{1 \times 3}, v_j] \cdot x &= v_j \cdot t_0, & \text{if } v_j \in V_t, \\ [v_j, 0_{1 \times 3}] \cdot x &= v_j \cdot r_0, & \text{if } v_j \in V_r. \end{aligned} \quad (13)$$

In order to solve the problem, the constraints have to be brought to a matrix form of $Cx = d$. The number of constraints corresponds to the amount of *none* and *partial* categories of each eigenvector. The number of constraints is denoted as m_t and m_r , with the total number of constraints $c = m_t + m_r \leq 6$. The constraints in the matrix form are:

$$\underbrace{\begin{bmatrix} 0_{m_r \times 3} & v_j \\ \vdots & \vdots \\ v_j & 0_{m_t \times 3} \end{bmatrix}}_{C_{(m_r+m_t) \times 6}} x = \underbrace{\begin{bmatrix} v_j \cdot r_0 \\ \vdots \\ v_j \cdot t_0 \end{bmatrix}}_{d_{(m_r+m_t) \times 1}}, \quad (14)$$

where each row indicates an equality constraint. The whole optimization can then be re-expressed as:

$$\begin{aligned} \min_{x \in \mathbb{R}^6} \quad & \|A'x - b'\|_2, \\ \text{s.t.} \quad & Cx - d = 0 \end{aligned} \quad (15)$$

where $C \in \mathbb{R}^{c \times 6}$ is the mapping matrix between the optimization variables x and the constraint $d \in \mathbb{R}^{c \times 1}$. The optimization (15) can be transferred into an unconstrained optimization problem by introducing Lagrangian multipliers [63]. The final augmented unconstrained linear least squares minimization problem then becomes:

$$\min_{x' \in \mathbb{R}^6} \|A''x' - b''\|_2, \quad (16)$$

where $x' = [x^{*\top}, \lambda^{*\top}]^\top$ is the augmented optimization vector with Lagrangian multipliers $\lambda \in \mathbb{R}^{c \times 1}$. A simplified example of the optimization is illustrated in Fig. 4-B, where a single planar constraint is shown, limiting the solution space. Furthermore, the augmented matrices in Equation (16) are defined as:

$$\underbrace{\begin{bmatrix} 2A^\top A & C^\top \\ C & 0 \end{bmatrix}}_{A''} \underbrace{\begin{bmatrix} x^* \\ \lambda^* \end{bmatrix}}_{x'} = \underbrace{\begin{bmatrix} 2A^\top b \\ d \end{bmatrix}}_{b''}.$$

This optimization problem can then be solved by using SVD, providing the pose estimation x' for the current ICP iteration.

VII. RESULTS

In this section, the experimental setup is discussed in Section VII-A, and the performance evaluation of the proposed framework is presented through Sections VII-C to VII-F. A video showcasing the robot field deployment and summarizing the proposed framework is provided online¹. Finally, to validate the efficacy of individual sub-modules of the proposed solution ablation studies are presented in Section VII-G.

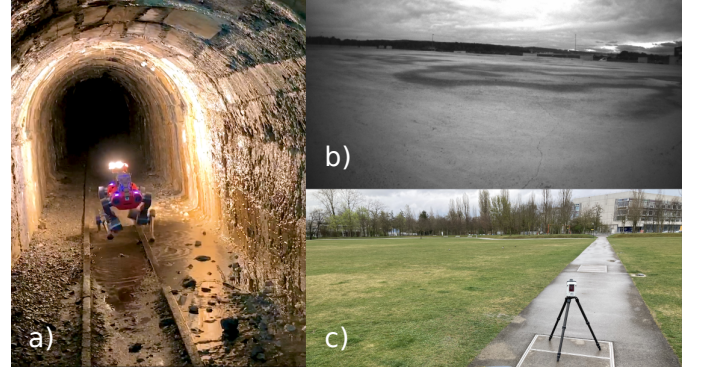


Fig. 5. Overview of the three real-world experiment sites. a) Deployed ANYmal in Seemühle Underground Mine. b) An on-board image of the Rümlang Construction Site showing the featureless open-space. c) Ground truth collection at Opfikon City Park with the RTC360 [64] sensor.

A. Hardware & Implementation Details

The proposed localizability-aware ICP framework is integrated into a C++ SLAM system, Pharos [58], [59], based on the popular open-source library *libpointmatcher* to demonstrate the benefits of the proposed approach in challenging real-world experiments. As the robot platform, the third generation of the ANYmal [65] series - ANYmal C shown in Fig. 1 top right and Fig. 5-(a, c) is equipped with a Velodyne VLP-16 LiDAR, configured to stream 360-degree point clouds at 10 Hz, an inertial measurement unit (IMU), and joint encoders. ANYmal's *legged odometry module* [66] utilizes the IMU and joint encoder measurements to calculate the initial transformation required by the ICP algorithm. In all of the real-world experiments, an ANYmal was used to collect data. All evaluations were performed on a laptop equipped with a processor Intel i7-9750H CPU, equivalent to that available on the robot.

B. State-of-the-Art Methods

To put X-ICP into the context of the existing scholarly works, a comparison against current state-of-the-art methods of Zhang et al. [15], and Hinduja et al. [24] is performed by re-implementing these methods within the same ICP framework as the proposed method for a fair comparison. The method of Zhang et al. [15] requires an eigenvalue threshold for degeneracy detection, and this threshold is set to 120 empirically to ensure a good degeneracy detection for all the experiments.

C. Simulation Study

To evaluate the localizability detection performance of the proposed method, first, a validation is performed in simulation to control the variables affecting ICP registration, such as providing a perfect prior and, hence, removing it as a source of error. In addition, the simulation environment, as shown in Fig. 6, is designed to feature smooth planar surfaces, self-similar corridors, and an open area - all providing challenging conditions known to induce ICP degeneracy.

During the test, the robot starts in a corridor-like area, navigates to an open space, and returns to the starting position, traversing a total distance of 246 m at a nominal velocity

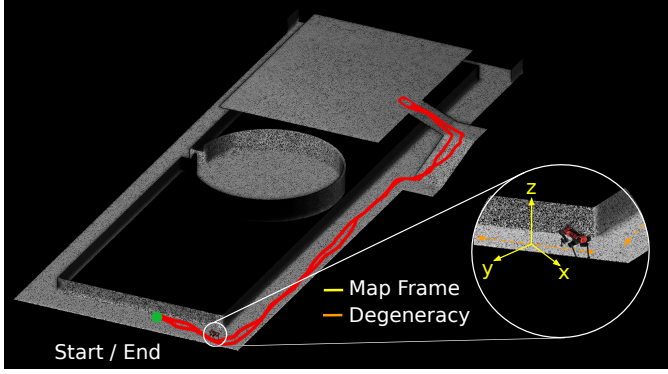


Fig. 6. The ground truth point cloud map of the simulation scene. The robot's path is depicted as a red line. The two degenerate directions and the misaligned map-frame are shown to highlight the importance of direction-invariant localizability detection in eigenspace.

of 0.5 m/s. In the corridor sections, the ICP registration is expected to degenerate in one axis along the length of the corridors. In contrast, in the open section, it is expected that the degeneracy would occur along two translational directions parallel to the ground plane and in one rotational direction along the axis perpendicular to the ground plane. The results in Fig. 7 validate the correct degeneracy detection performance of the proposed work as non-localizability is detected along one axis throughout the test, corresponding to corridor sections. Furthermore, non-localizability along two additional axes is only detected for the 200-300s mark, corresponding to the open section of the environment. The performance of the proposed method is also compared to the two state-of-the-art methods, and a comparison of maps generated by the three methods is presented in Fig. 7. It should be noted that in this simulation experiment, a perfect prior is available. The method of Hinduja et al. [24] remains overly pessimistic and relies on ICP pose prior to do registration showing less drift than Zhang et al. [15], which remains overly optimistic in the detection of rotation degeneracy, hence leading to the incorrect map. Importantly, these methods do not make use of the partial localizability information available along the degenerate directions as done by the proposed method, which shows minimal map error w.r.t ground-truth.

D. Seemühle Underground Mine

During this test, ANYmal traversed an abandoned underground mine in Switzerland, containing multiple challenges. First, the ground of the mine is populated with rocks and sharp objects, leading to foot slip, affecting the reliable ground contact estimation used by the legged odometry prior [66]. Second, the environment contains a long tunnel segment with smooth-arched walls (cf. Fig. 5-a and Fig. 1-A, B, C) that do not provide reliable constraints along the longitudinal direction of the tunnel. The ground truth point cloud map of the environment was obtained using a Leica RTC 360 scanner (cf. Fig. 1) and used to generate ground truth robot trajectory using the method in [67]. The same experiment was performed twice on ANYmal; once with a Velodyne VLP-16, and once with an Ouster OS0-128, allowing for a comparative analysis of the

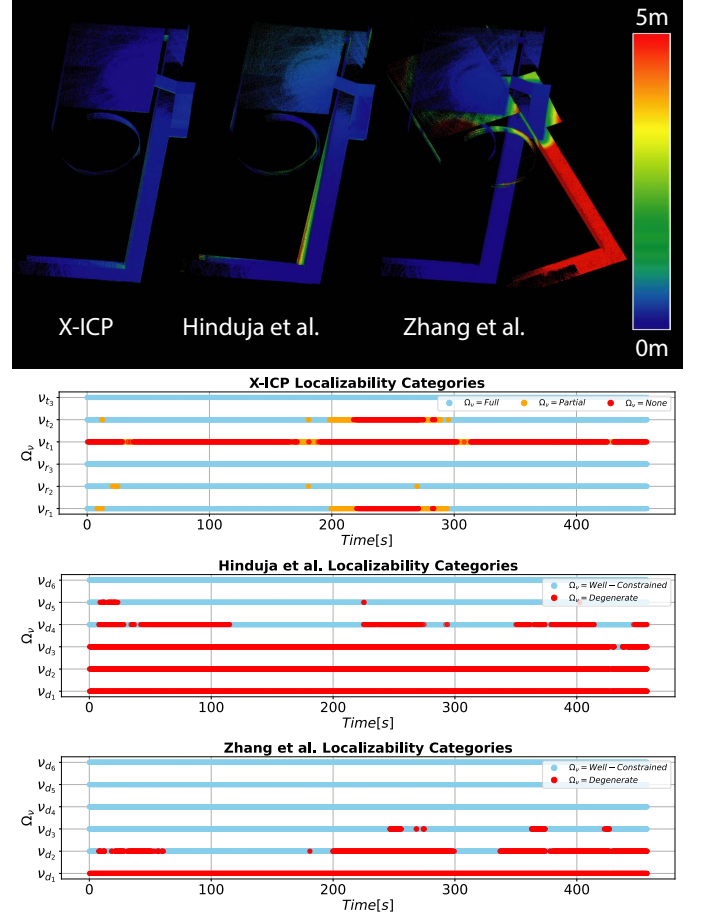


Fig. 7. **Top:** The generated point cloud maps of the simulation environment are shown. **Bottom:** The estimated localizability categories by X-ICP and the state-of-the-art methods are provided. Note, that other methods significantly suffer from the perfectly planar walls in simulation.

effect of different point cloud density and FoV configurations on the proposed method. The robot traversed a total distance of 521.8 m during this experiment.

1) *Velodyne VLP-16:* The error heat maps of the three methods for the experiment conducted with the Velodyne VLP-16 LiDAR sensor are shown in the bottom row of Fig. 1. Both state-of-the-art approaches suffer from the impact of environmental degeneracy, prohibiting a drift-free traversal. The method of Zhang et al. [15] performs comparably to the proposed solution until the robot observes the tunnel for the second time on the way back. During the traversal of the way back, the binary detection performs sub-optimally, resulting in LiDAR slip. Moreover, the solution of Hinduja et al. [24] leads to a larger registration error throughout the experiment, as depicted in the error heat map, due to a pessimistic condition number-based threshold. Hence, wrongfully used legged odometry prior suffers from slip and imprecision in multiple instances, leading to a broken final point cloud map. On the other hand, X-ICP performs reliable and consistent registration throughout the tunnel segment, keeping the point cloud map unimpaired. The mapping result of the simplified version of the proposed algorithm, Xs-ICP, is discussed in Section VII-G as an ablation study and shown in Fig. 15.

The corresponding localizability estimation is shown in

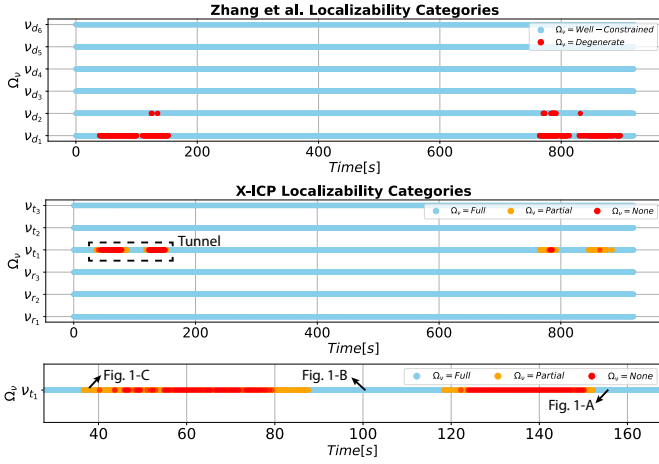


Fig. 8. Localizability predictions of different methods for the Seemühle VLP-16 experiment are shown. **Top:** Localizability categories by Zhang et al. [15]. **Middle:** Detected localizability categories of the proposed X-ICP. **Bottom:** Zoomed-in X-ICP localizability categories of the tunnel segment.

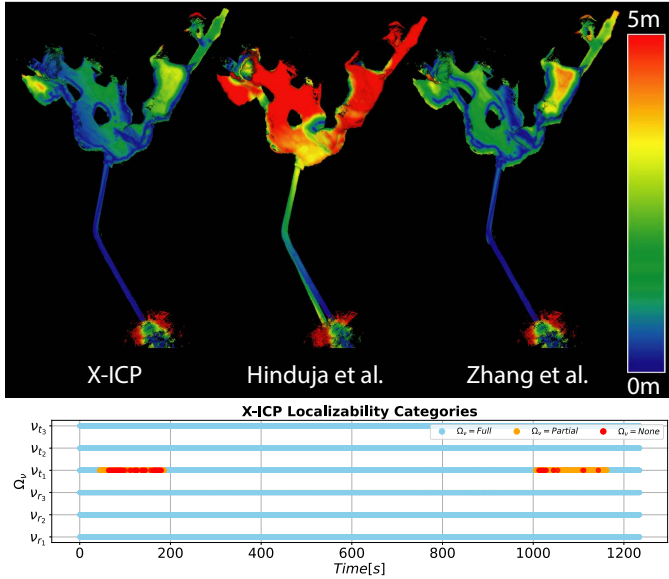


Fig. 9. **Top Row:** Point cloud maps of the three approaches for the Seemühle experiment with Ouster OS0-128 LiDAR sensor are illustrated. **Bottom Row:** Detected localizability categories by X-ICP are shown.

Fig. 8. In the top row the localizability categories of X-ICP show how the Loc.-Module captures the tunnel section at the beginning and end of the Seemühle VLP-16 test. Here, the advantage of detecting localizability in eigenspace can be seen; although the robot moves and rotates within the environment, the degeneracy only affects a single direction of the motion, in this case, v_{t_1} . Since this vector is defined in the eigenspace, it does not need to align with any of the Cartesian axes in the ICP or optimization frame. In the bottom row of Fig. 8, a close-up of the localizability detection in the tunnel is provided. Remarkably, the correspondence of the localizability detection to certain parts of the tunnels reveals that the three-level detection can distinguish the subtle differences in localizability at the turn of the tunnel point B in Fig. 1, allowing the optimization to utilize the point cloud information for more controlled localization.

To present numerical comparisons, the absolute pose error (APE), relative pose error (RPE) [68], and end position errors are calculated using the EVO evaluation package³. APE is a measure of the global consistency of the estimated robot trajectory. Results for two different trajectory alignment methods are reported (cf. Table I):

- 1) Alignment of the first 15 m of the trajectory with the ground truth trajectory. This 15 m segment is selected to include the beginning of the tunnel while excluding the non-localizable sections.
- 2) The origin alignment method of EVO, which aligns the first pose of the ground truth and the estimated poses.

TABLE I
APE ERROR FOR SEEMÜHLE MINE EXPERIMENT WITH VLP-16 (BEST IN **BOLD**).

	First 15 m Alignment		Origin Alignment		
	Translation $\mu(\sigma)[m]$	Rotation $\mu(\sigma)[deg]$	Translation $\mu(\sigma)[m]$	Rotation $\mu(\sigma)[deg]$	Last Position Error[m]
X-ICP (Proposed)	2.05 (1.23)	2.55 (0.76)	2.45 (1.35)	2.50 (1.03)	0.27
Xs-ICP (Proposed)	2.29(1.22)	3.06(1.19)	2.68(1.26)	3.08(1.3)	5.34
Zhang et al. [15]	3.36(1.74)	4.06(1.37)	3.73(1.80)	4.11(1.52)	6.37
Hinduja et al. [24]	5.79(5.26)	7.67(4.72)	8.16(4.83)	8.03(4.73)	24.17

In addition to the APE, also the end position error is calculated as the difference between the last estimated robot position and the ground truth position. The results indicate that the state-of-the-art methods globally drift, whereas the proposed solution can keep the point cloud map unimpaired. Both the APE metric and the end translation errors in Table I show the reduced global drift of the proposed method and its fast variant. Additionally, the RPE error is investigated to analyze local pose estimation accuracy and measure the relative pose drift (cf. Table II). The results shown in Table II unveil that

TABLE II
RPE PER 10 m TRAVERSED DISTANCE FOR SEEMÜHLE MINE EXPERIMENT WITH VLP-16 (BEST IN **BOLD**).

	Translation $\mu(\sigma)[m]$	Rotation $\mu(\sigma)[deg]$
X-ICP (Proposed)	0.17 (0.12)	0.86(0.42)
Xs-ICP (Proposed)	0.19(0.13)	0.85 (0.47)
Zhang et al. [15]	0.20(0.14)	0.93(0.51)
Hinduja et al. [24]	0.26(0.14)	1.28(0.74)

the proposed method and its fast variant perform better than the state-of-the-art methods in local consistency.

2) *Ouster OS0-128*: To investigate the robustness and applicability of the proposed approach to different sensor setups, the tests are repeated with the data from an Ouster OS0-128 LiDAR with a much higher point density and FoV at the cost of higher noise. To accommodate this increase in sensor noise, the filtering threshold κ_f is reduced to 60° . As seen in the top row of Fig. 9, the state-of-the-art approaches benefit

³<https://github.com/MichaelGrupp/evo>

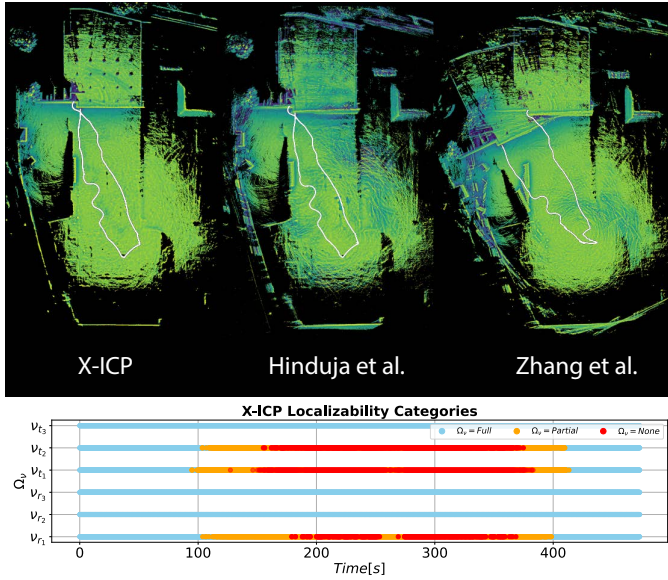


Fig. 10. **Top Row:** Point cloud maps of X-ICP and the two state-of-the-art approaches for the Rumläng experiment. **Bottom Row:** Predicted localizability categories of X-ICP.

from this higher richness in information and perform better overall than with the VLP-16. Despite the improvement over the results from the VLP-16 experiment, the solution from Hinduja et al. [24] still performs sub-optimally and generates a perceptually degenerate map. On the other hand, Zhang et al. [15] can complete the trajectory without substantial drift. Moreover, also the proposed X-ICP benefits from the denser point clouds. Interestingly, X-ICP registered map has less drift at the inner parts of the cave. In addition, the localizability categories are shown at the bottom row of Fig. 9. Here, similar to before, the degeneracy in the tunnel section of the environment is well-captured. Differently, despite the similarity of the environment, the information observed by the ICP optimization differs from the VLP-16 experiment leading to different degeneracy characteristics.

E. Rumläng Construction Site

In this field test, the robot navigated a construction site at Rumläng, Switzerland, shown in Fig. 5-b, which represents an open environment with limited structure, thus presenting an under-constrained scenario for translation along the ground plane and rotation perpendicular to plane. During the test, the robot started next to a garage-like structure before traversing to an open area and performed a couple of in-spot rotations before returning back, traversing a total distance of 153 m. The in-spot rotations in the open space were performed to stress test the yaw estimation performance of the registration methods.

The experiment results and comparison to state-of-the-art methods are presented in Fig. 10, with the top row showcasing the effect of using different localizability detection methods to generate a point cloud map of the environment. It can be seen that relying on the method by Zhang et al. [15] leads to poor performance. This is because its degeneracy detection relies on the eigenvalues of the optimization; however, this

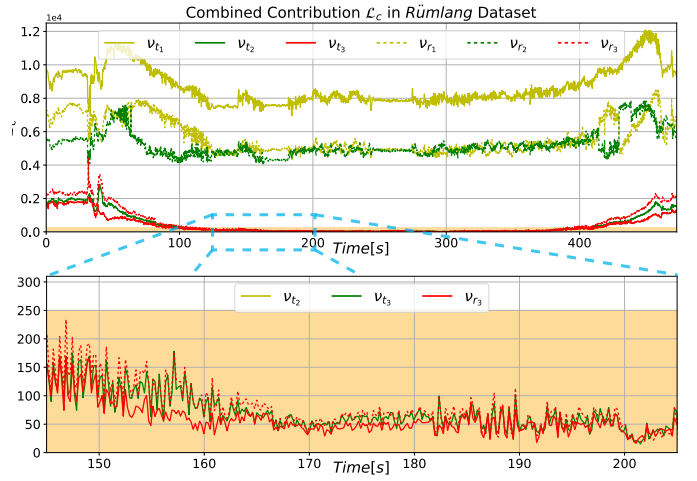


Fig. 11. **Top Row:** Change of \mathcal{L}_c throughout the Rumläng experiment. The shaded orange region (zoomed-in in **Bottom Row**) represents the active region of the localizability awareness.

parameterization does not allow for the detection of rotation and translation degeneracy with a single threshold, as the scale of eigenvalues between rotation and translation sub-spaces differ significantly. The method by Hinduja et al. [24] seems to perform much better as due to its pessimistic localizability detection for pose estimation, it relies more on the legged odometry prior, which performs well in this environment. However, upon closer observation, map distortion in the form of blurry rigid structures can be noted due to errors accumulated from the drift in the pose prior. In contrast, the proposed method produces a consistent map of the environment preserving fine details, with its localizability detection performance shown in the bottom row of Fig. 10. It can be noted that not only X-ICP is able to correctly detect non-localizability along the three degenerate directions in the open area, but captures the smooth transition between partial and non-localizability.

The smooth change of the localizability categories can be better understood by observing the combined contribution change given in Fig. 11. In this figure, the degenerate directions are easily identifiable with their comparably low combined contribution value.

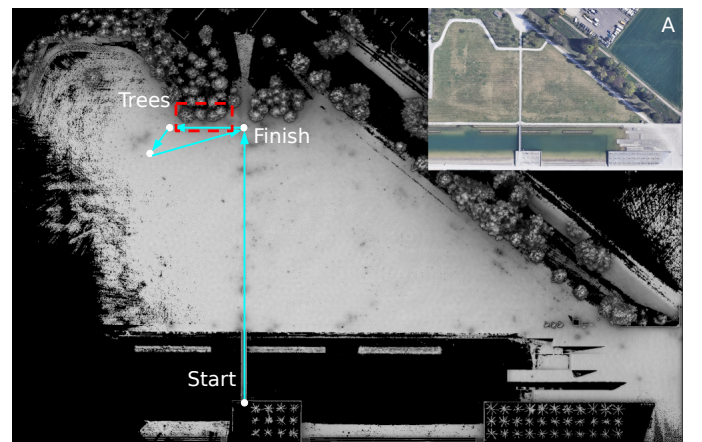


Fig. 12. Ground truth point cloud map of the Opfikon City Park. The highlighted trees are later investigated in 14 as a demonstration of the effectiveness of X-ICP. **Image A:** Satellite view of the Opfikon City Park.

F. Opfikon City Park

To test the efficacy of the proposed method in natural environments containing trees and grass, a test was conducted in a park at Opfikon, Switzerland. In this test, the robot traversed over soft terrain and a suspension metal bridge, both of which adversely affected the legged odometry prior used for point cloud registration. In addition, the vegetation-covered terrain made it difficult to extract the surface-normals reliably - making pose estimation challenging. Furthermore, towards the end, the robot enters an open unstructured area near the center of the park, presenting a LiDAR degenerate environment. During this test, the robot traversed a total distance of 235 m, and the ground truth map of the environment, shown in Fig. 12, is collected using a Leica RTC 360 scanner as shown in Fig. 5-c.

Unlike the previous tests, in this environment, the degeneracy detection threshold of Zhang et al. [15] is adapted to investigate the effect of heuristic-tuning. Fig. 13 demonstrates the effect of choosing the correct threshold. It can be understood that an incorrect threshold can completely degrade the quality of the map. As a result, to make the comparison in favour of the state-of-the-art method, the threshold is tuned to be 200, an increment from the default 120.

A quantitative comparison of the proposed method to the ground truth map and the state-of-the-art methods is presented in Fig. 14. Looking at the zoomed-in in-set images, it can be noted that the proposed method produces the most accurate map reconstruction and preserves finer details of the trees without needing any heuristic re-tuning. The error heat map shows that the approach of Hinduja et al. [24], which remains over pessimistic, drifts significantly in the presence of degraded prior information. This result highlights the consistent performance of the proposed method across natural and man-made environments and emphasizes the need for more robust and heuristic-free generalizable localizability detection methods.

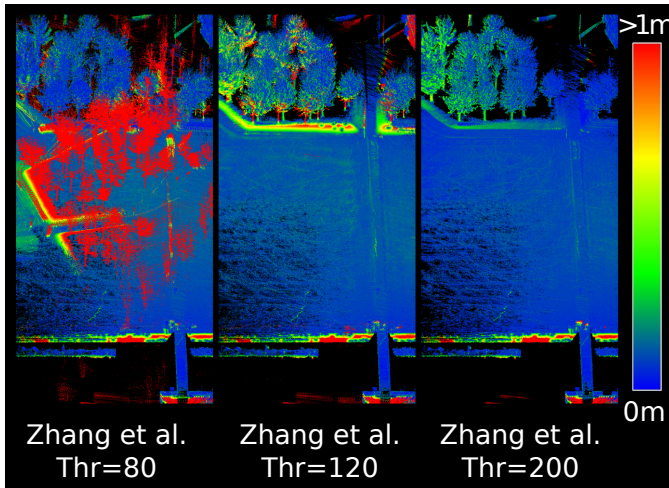


Fig. 13. Point cloud maps of the approach by Zhang et al. [15] for different eigenvalue thresholds for the Opfikon City Park experiment.

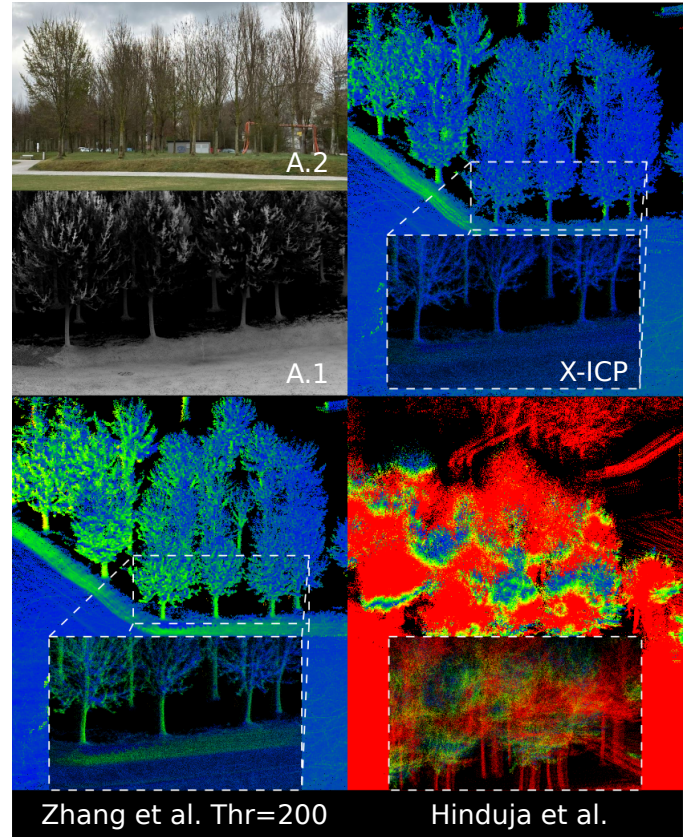


Fig. 14. Zoomed-in point cloud maps of X-ICP and the other two approaches for the Opfikon City Park experiment (cf. Fig. 12). The error color-scale is identical to Fig. 13. Image A.1 and A.2 depict the real picture and ground truth for the tree region, respectively.

G. Ablation Studies

The results discussed in the previous section validate the advantage of employing X-ICP in different LiDAR-challenging environments. To better understand the origin of the achieved improvements, the effect of different components of the proposed method is investigated in an ablation study. In particular, X-ICP and Xs-ICP are researched and compared in view of the localizability analysis; mainly looking at the three-level analysis and the importance of conducting the analysis in every iteration of ICP.

1) *Seemühle*: Firstly, different versions of the proposed solution are tested on the Seemühle VLP-16 experiment, with results shown in Fig. 15. An increase in the robot pose drift is apparent when *partial-localizability* is disabled (*Xs-ICP*), implying that using the three-level detection can lead to a better registration. The localizability detection of the two variants is studied in the bottom plot of Fig. 15. In particular, when traversing the tunnel for the second time, the *partial-localizability* dominates, while *Xs-ICP* estimates the localizability as non-localizable and fully relies on the prior for this eigenvector direction.

2) *Rümlang*: Secondly, a similar study is done for the Rümlang experiment, and the results are shown in Fig. 16. While the mapping performance of both proposed methods is satisfactory, the walls are registered twofold for *Xs-ICP*, indicating a slight LiDAR-slip in rotation. Consequently, *partial-*

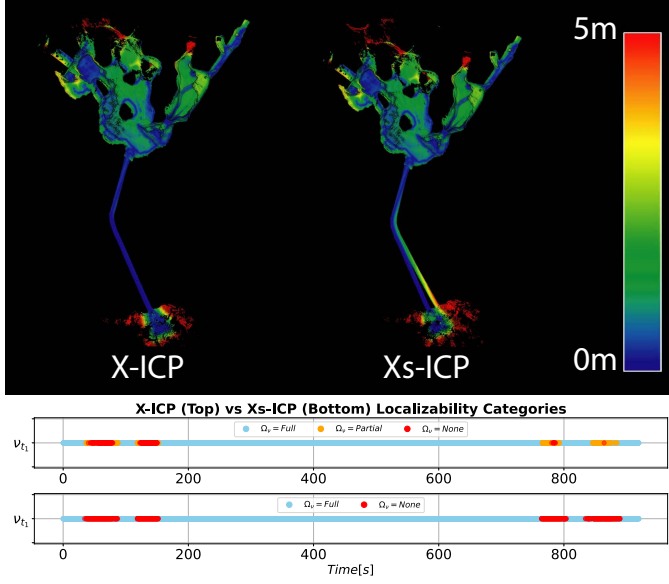


Fig. 15. **Top Row:** Point cloud maps of the proposed X-ICP and Xs-ICP for the Seemühle experiment, using the VLP-16 LiDAR. **Bottom Row:** Predicted localizability categories of the tunnel section for X-ICP and Xs-ICP.

localizability improves localizability estimation and mapping performance also for this case. A snapshot of the localizability analysis at point A is shown in the lower part of Fig. 16, illustrating the found partial-localizability for one of the directions. The histograms show three directions, two of these directions are shown as yellow arrows in the bottom right image, which are the non-localizable translation directions, while the partially-localizable rotation direction is indicated by the blue arrow. The partially-localizable direction can be explained by the few but highly informative information pairs seen at the bottom right histogram, which are then utilized in the optimization as constraints.

3) *Scalability:* Lastly, a scalability analysis is performed to evaluate the computational overhead of different methods. The analysis determines the overhead per ICP iteration versus the number of found matches, shown in Fig. 17. The method of Zhang et al. [15] is not shown here as its analysis is only required to run once at the beginning of the ICP optimization and creates less overhead than the shown methods.

Here, the overhead of X-ICP is analyzed for one and three DoF degeneracy, the most common cases in real-world deployments. Since Xs-ICP does not require any re-sampling of points, the shown line represents all conditions. Both X-ICP and Xs-ICP methods are real-time applicable for cases ranging from sparse 16-ray LiDARs to dense 128-ray LiDARs. By design, Xs-ICP requires less computation than X-ICP, yet, it is still taking more computational resources than the state-of-the-art methods.

VIII. CONCLUSION AND FUTUREWORK

This work presented a localizability awareness system to enable robust and reliable pose estimation in LiDAR-based registration. The proposed approach detects LiDAR degeneracy in the ICP algorithm and constrains the subsequent optimization to only allow for motion updates along healthy

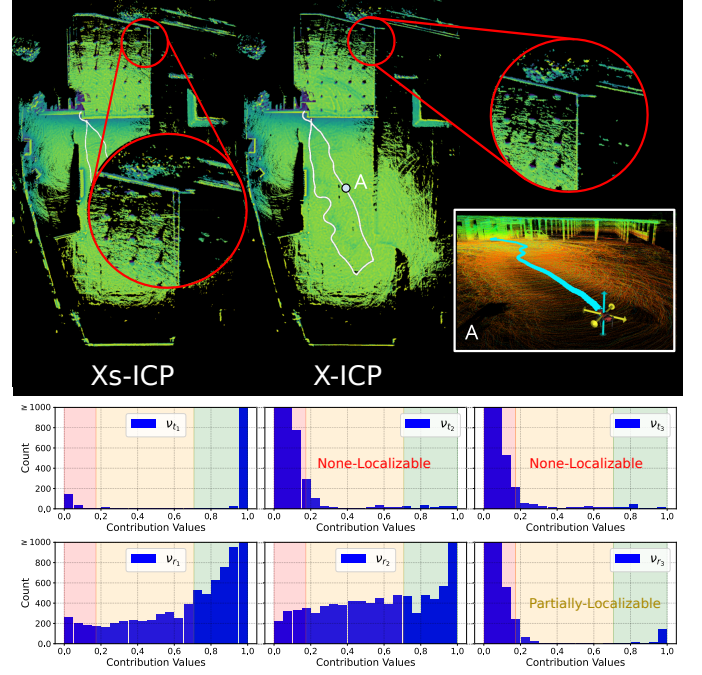


Fig. 16. **Top:** Point cloud maps of X-ICP and Xs-ICP approaches of the Rümmlang test site. A close-up of point A is shown to illustrate the detected degeneracy (arrows). **Bottom:** Contribution values are shown for point A as processed by X-ICP. Note that two directions are non-localizable, while one is partially localizable.

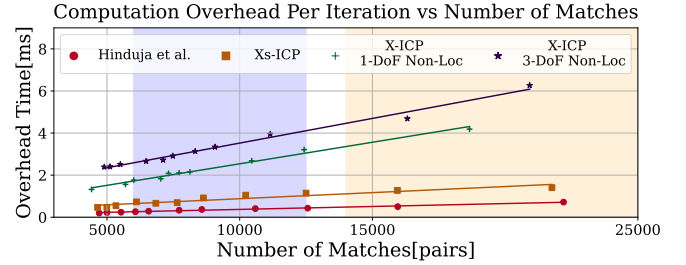


Fig. 17. Scalability analysis of proposed solutions and the method by Hinduja et al. [24]. The purple region () roughly covers the number of matches present for a VLP-16 LiDAR. The light-orange region () represents the number of possible matches of an Ouster OS0-128 LiDAR.

directions. The efficacy of the presented approach is demonstrated through three real-world examples and a simulation-based analysis, all containing ill-conditioned ICP-based pose estimation. Furthermore, thorough analyses and an ablation study showcase the applicability and performance of individual parts of the proposed pipeline. Considering the possible limitations of only incorporating equality constraints into the optimization, one promising topic for future research is the integration of inequality constraints into the localizability-aware ICP to relax the optimization process. Moreover, the sensor-dependent selection process of κ_1 is planned to be improved by introducing a confidence filter that would assign point-wise confidence values to the pairs as weights to reduce the effect of noise on the contribution calculation. Finally, to enrich the utilization of the proposed fine-grained localizability, the presented work will be integrated into a graph-based robust and degeneracy-aware sensor fusion framework [69] in the form of partial factors [24].

ACKNOWLEDGMENT

The authors thank Marco Tranzatto, Samuel Zimmerman, Timon Homberger and Alexander Reske for their valuable support during the collection of datasets. Additionally, the authors thank the ANYbotics perception team for the technical discussions and practical considerations.

REFERENCES

- [1] R. Latif, K. Dahmane, and A. Saddik, "Slam algorithm: Overview and evaluation in a heterogeneous system," *Enabling Machine Learning Applications in Data Science*, pp. 165–177, 2021.
- [2] C. Cadena, L. Carlone, H. Carrillo, Y. Latif, D. Scaramuzza, J. Neira, I. Reid, and J. J. Leonard, "Past, present, and future of simultaneous localization and mapping: Toward the robust-perception age," *IEEE Transactions on robotics*, vol. 32, no. 6, pp. 1309–1332, 2016.
- [3] K. Ebadi, L. Bernreiter, H. Biggie, G. Catt, Y. Chang, A. Chatterjee, C. E. Denniston, S.-P. Deschênes, K. Harlow, S. Khattak, *et al.*, "Present and future of slam in extreme underground environments," *arXiv preprint arXiv:2208.01787*, 2022.
- [4] A. Geiger, P. Lenz, and R. Urtasun, "Are we ready for autonomous driving? the kitti vision benchmark suite," in *2012 IEEE conference on computer vision and pattern recognition*. IEEE, 2012, pp. 3354–3361.
- [5] M. Helmberger, K. Morin, B. Berner, N. Kumar, G. Cioffi, and D. Scaramuzza, "The hilti slam challenge dataset," *IEEE Robotics and Automation Letters*, vol. 7, no. 3, pp. 7518–7525, 2022.
- [6] P. J. Besl and N. D. McKay, "Method for registration of 3-d shapes," in *Sensor fusion IV: control paradigms and data structures*, vol. 1611. Spie, 1992, pp. 586–606.
- [7] K.-L. Low, "Linear least-squares optimization for point-to-plane icp surface registration," *Chapel Hill, University of North Carolina*, vol. 4, no. 10, pp. 1–3, 2004.
- [8] J. Zhang and S. Singh, "Loam: Lidar odometry and mapping in real-time," in *Robotics: Science and Systems*, vol. 2, no. 9. Berkeley, CA, 2014, pp. 1–9.
- [9] J. Behley and C. Stachniss, "Efficient surfel-based slam using 3d laser range data in urban environments," in *Robotics: Science and Systems*, vol. 2018, 2018, p. 59.
- [10] M. Tranzatto, T. Miki, M. Dharmadhikari, L. Bernreiter, M. Kulkarni, F. Mascarich, O. Andersson, S. Khattak, M. Hutter, R. Siegwart, and K. Alexis, "Cerberus in the darpa subterranean challenge," *Science Robotics*, vol. 7, no. 66, p. eabp9742, 2022.
- [11] I. Vizzo, T. Guadagnino, B. Mersch, L. Wiesmann, J. Behley, and C. Stachniss, "Kiss-icp: In defense of point-to-point icp—simple, accurate, and robust registration if done the right way," *arXiv preprint arXiv:2209.15397*, 2022.
- [12] E. Jelavic, J. Nubert, and M. Hutter, "Open3d slam: Point cloud based mapping and localization for education," in *Robotic Perception and Mapping: Emerging Techniques, ICRA 2022 Workshop*. ETH Zurich, Robotic Systems Lab, 2022, p. 24.
- [13] A. Censi, "An accurate closed-form estimate of icp's covariance," in *Proceedings 2007 IEEE international conference on robotics and automation*. IEEE, 2007, pp. 3167–3172.
- [14] M. Brossard, S. Bonnabel, and A. Barrau, "A new approach to 3d icp covariance estimation," *IEEE Robotics and Automation Letters*, vol. 5, no. 2, pp. 744–751, 2020.
- [15] J. Zhang, M. Kaess, and S. Singh, "On degeneracy of optimization-based state estimation problems," in *2016 IEEE International Conference on Robotics and Automation (ICRA)*. IEEE, 2016, pp. 809–816.
- [16] J. Nubert, S. Khattak, and M. Hutter, "Self-supervised learning of lidar odometry for robotic applications," in *2021 IEEE International Conference on Robotics and Automation (ICRA)*, 2021, pp. 9601–9607.
- [17] J. Nubert, E. Walther, S. Khattak, and M. Hutter, "Learning-based localizability estimation for robust lidar localization," in *IEEE/RSJ International Conference on Intelligent Robots and Systems (IROS)*. IEEE, 2022.
- [18] W. Zhen, S. Zeng, and S. Soberer, "Robust localization and localizability estimation with a rotating laser scanner," in *2017 IEEE International Conference on Robotics and Automation (ICRA)*. IEEE, 2017, pp. 6240–6245.
- [19] W. Zhen and S. Scherer, "Estimating the localizability in tunnel-like environments using lidar and uwb," in *2019 International Conference on Robotics and Automation (ICRA)*. IEEE, 2019, pp. 4903–4908.
- [20] S. Nobili, G. Tinchev, and M. Fallon, "Predicting alignment risk to prevent localization failure," in *2018 IEEE International Conference on Robotics and Automation (ICRA)*. IEEE, 2018, pp. 1003–1010.
- [21] M. Ramezani, G. Tinchev, E. Iuganov, and M. Fallon, "Online lidar-slam for legged robots with robust registration and deep-learned loop closure," in *2020 IEEE International Conference on Robotics and Automation (ICRA)*. IEEE, 2020, pp. 4158–4164.
- [22] A. Tagliabue, J. Tordesillas, X. Cai, A. Santamaria-Navarro, J. P. How, L. Carlone, and A.-a. Agha-mohammadi, "Lion: Lidar-inertial observability-aware navigator for vision-denied environments," in *International Symposium on Experimental Robotics*. Springer, 2020, pp. 380–390.
- [23] Y. Liu, J. Wang, and Y. Huang, "A localizability estimation method for mobile robots based on 3d point cloud feature," in *2021 IEEE International Conference on Real-time Computing and Robotics (RCAR)*. IEEE, 2021, pp. 1035–1041.
- [24] A. Hinduja, B.-J. Ho, and M. Kaess, "Degeneracy-aware factors with applications to underwater slam," in *2019 IEEE/RSJ International Conference on Intelligent Robots and Systems (IROS)*. IEEE, 2019, pp. 1293–1299.
- [25] P. Biber and W. Straßer, "The normal distributions transform: A new approach to laser scan matching," in *Proceedings 2003 IEEE/RSJ International Conference on Intelligent Robots and Systems (IROS 2003)(Cat. No. 03CH37453)*, vol. 3. IEEE, 2003, pp. 2743–2748.
- [26] A. Segal, D. Haehnel, and S. Thrun, "Generalized-icp," in *Robotics: science and systems*, vol. 2, no. 4. Seattle, WA, 2009, p. 435.
- [27] F. Pomerleau, "Applied registration for robotics: Methodology and tools for icp-like algorithms," Ph.D. dissertation, ETH Zurich, 2013.
- [28] A. Censi, "An icp variant using a point-to-line metric," in *2008 IEEE International Conference on Robotics and Automation*. IEEE, 2008, pp. 19–25.
- [29] P. Babin, P. Dandurand, V. Kubelka, P. Giguère, and F. Pomerleau, "Large-scale 3d mapping of subarctic forests," in *Field and Service Robotics*. Springer, 2021, pp. 261–275.
- [30] S. Rusinkiewicz, "A symmetric objective function for icp," *ACM Transactions on Graphics (TOG)*, vol. 38, no. 4, pp. 1–7, 2019.
- [31] M. Yokozuka, K. Koide, S. Oishi, and A. Banno, "Litamin2: Ultra light lidar-based slam using geometric approximation applied with kl-divergence," in *2021 IEEE International Conference on Robotics and Automation (ICRA)*. IEEE, 2021, pp. 11 619–11 625.
- [32] M. Ramezani, K. Khosoussi, G. Catt, P. Moghadam, J. Williams, P. Borges, F. Pauling, and N. Kottege, "Wildcat: Online continuous-time 3d lidar-inertial slam," *arXiv preprint arXiv:2205.12595*, 2022.
- [33] S. Khattak, H. Nguyen, F. Mascarich, T. Dang, and K. Alexis, "Complementary multi-modal sensor fusion for resilient robot pose estimation in subterranean environments," in *2020 International Conference on Unmanned Aircraft Systems (ICUAS)*. IEEE, 2020, pp. 1024–1029.
- [34] K. Ebadi, M. Palieri, S. Wood, C. Padgett, and A.-a. Agha-mohammadi, "Dare-slam: Degeneracy-aware and resilient loop closing in perceptually-degraded environments," *Journal of Intelligent & Robotic Systems*, vol. 102, no. 1, pp. 1–25, 2021.
- [35] D. Landry, F. Pomerleau, and P. Giguère, "Cello-3d: Estimating the covariance of icp in the real world," in *2019 International Conference on Robotics and Automation (ICRA)*. IEEE, 2019, pp. 8190–8196.
- [36] A. De Maio and S. Lacroix, "Deep bayesian icp covariance estimation," *arXiv preprint arXiv:2202.11607*, 2022.
- [37] S. Bonnabel, M. Barczyk, and F. Goulette, "On the covariance of icp-based scan-matching techniques," in *2016 American Control Conference (ACC)*. IEEE, 2016, pp. 5498–5503.
- [38] N. Gelfand, L. Ikemoto, S. Rusinkiewicz, and M. Levoy, "Geometrically stable sampling for the icp algorithm," in *Fourth International Conference on 3-D Digital Imaging and Modeling, 2003. 3DIM 2003. Proceedings*. IEEE, 2003, pp. 260–267.
- [39] T.-H. Kwok and K. Tang, "Improvements to the iterative closest point algorithm for shape registration in manufacturing," *Journal of Manufacturing Science and Engineering*, vol. 138, no. 1, 2016.
- [40] J.-E. Deschaud, "Imls-slam: Scan-to-model matching based on 3d data," in *2018 IEEE International Conference on Robotics and Automation (ICRA)*. IEEE, 2018, pp. 2480–2485.
- [41] Z. Rong and N. Michael, "Detection and prediction of near-term state estimation degradation via online nonlinear observability analysis," in *2016 IEEE International Symposium on Safety, Security, and Rescue Robotics (SSRR)*. IEEE, 2016, pp. 28–33.
- [42] H. Cho, S. Yeon, H. Choi, and N. Doh, "Detection and compensation of degeneracy cases for imu-kinect integrated continuous slam with plane features," *Sensors*, vol. 18, no. 4, p. 935, 2018.

- [43] L. Dong, W. Chen, and J. Wang, "Efficient feature extraction and localizability based matching for lidar slam," in *2021 IEEE International Conference on Robotics and Biomimetics (ROBIO)*. IEEE, 2021, pp. 820–825.
- [44] S. B. Nashed, J. J. Park, R. Webster, and J. W. Durham, "Robust rank deficient slam," in *IEEE/RSJ International Conference on Intelligent Robots and Systems (IROS)*. IEEE, 2021, pp. 6603–6608.
- [45] M. L. R. Arévalo, "On the uncertainty in active slam: representation, propagation and monotonicity," Ph.D. dissertation, Universidad de Zaragoza, 2018.
- [46] J. Jiao, H. Ye, Y. Zhu, and M. Liu, "Robust odometry and mapping for multi-lidar systems with online extrinsic calibration," *IEEE Transactions on Robotics*, 2021.
- [47] E. Westman and M. Kaess, "Degeneracy-aware imaging sonar simultaneous localization and mapping," *IEEE Journal of Oceanic Engineering*, vol. 45, no. 4, pp. 1280–1294, 2019.
- [48] R. Ren, H. Fu, H. Xue, Z. Sun, K. Ding, and P. Wang, "Towards a fully automated 3d reconstruction system based on lidar and gnss in challenging scenarios," *Remote Sensing*, vol. 13, no. 10, p. 1981, 2021.
- [49] H. Zhou, Z. Yao, and M. Lu, "Lidar/uvw fusion based slam with anti-degeneration capability," *IEEE Transactions on Vehicular Technology*, vol. 70, no. 1, pp. 820–830, 2020.
- [50] Y. Gao, S. Q. Wang, J. H. Li, M. Q. Hu, H. Y. Xia, H. Hu, and L. J. Wang, "A prediction method of localizability based on deep learning," *IEEE Access*, vol. 8, pp. 110 103–110 115, 2020.
- [51] S. Floery, "Constrained matching of point clouds and surfaces (ph. d. thesis)," *Technische Universität Wien*, 2010.
- [52] C. Olsson and A. Eriksson, "Solving quadratically constrained geometrical problems using lagrangian duality," in *2008 19th International Conference on Pattern Recognition*. IEEE, 2008, pp. 1–5.
- [53] S. Bouaziz, A. Tagliasacchi, and M. Pauly, "Sparse iterative closest point," in *Computer graphics forum*, vol. 32, no. 5. Wiley Online Library, 2013, pp. 113–123.
- [54] P. Dellenbach, J.-E. Deschaud, B. Jacquet, and F. Goulette, "Ct-icp: Real-time elastic lidar odometry with loop closure," in *2022 International Conference on Robotics and Automation (ICRA)*. IEEE, 2022, pp. 5580–5586.
- [55] H. Yang, J. Shi, and L. Carlone, "Teaser: Fast and certifiable point cloud registration," *IEEE Transactions on Robotics*, vol. 37, no. 2, pp. 314–333, 2020.
- [56] M. E. Wall, A. Rechtsteiner, and L. M. Rocha, "Singular value decomposition and principal component analysis," in *A practical approach to microarray data analysis*. Springer, 2003, pp. 91–109.
- [57] F. Pomerleau, F. Colas, R. Siegwart, et al., "A review of point cloud registration algorithms for mobile robotics," *Foundations and Trends® in Robotics*, vol. 4, no. 1, pp. 1–104, 2015.
- [58] Y. Nava, T. Tuna, G. Zhou, D. L. Madrid, M. Gaertner, M. Wulf, C. Gehring, and R. Diethelm, "Lidar-inertial odometry," ANYbotics, Report, 2022. [Online]. Available: <http://hdl.handle.net/20.500.11850/580200>
- [59] F. Pomerleau, F. Colas, R. Siegwart, and S. Magnenat, "Comparing icp variants on real-world data sets," *Autonomous Robots*, vol. 34, no. 3, pp. 133–148, 2013.
- [60] T.-H. Kwok, "Dnss: Dual-normal-space sampling for 3-d icp registration," *IEEE Transactions on Automation Science and Engineering*, vol. 16, no. 1, pp. 241–252, 2018.
- [61] C. Fu, X. Jiao, and T. Yang, "Efficient sparse lu factorization with partial pivoting on distributed memory architectures," *IEEE Transactions on Parallel and Distributed Systems*, vol. 9, no. 2, pp. 109–125, 1998.
- [62] M. Benzi and M. Tüma, "A robust incomplete factorization preconditioner for positive definite matrices," *Numerical Linear Algebra with Applications*, vol. 10, no. 5-6, pp. 385–400, 2003.
- [63] D. P. Bertsekas, *Constrained optimization and Lagrange multiplier methods*. Academic press, 2014.
- [64] A. Biasion, T. Moerwald, B. Walser, and G. Walsh, "A new approach to the terrestrial laser scanner workflow: the rtc360 solution," *FIG Working Week 2019: Geospatial Information for a Smarter Life and Environmental Resilience*, 2019.
- [65] M. Hutter, C. Gehring, A. Lauber, F. Gunther, C. D. Bellicoso, V. Tsounis, P. Fankhauser, R. Diethelm, S. Bachmann, M. Blösch, et al., "Anymal-toward legged robots for harsh environments," *Advanced Robotics*, vol. 31, no. 17, pp. 918–931, 2017.
- [66] M. Bloesch, M. Burri, H. Sommer, R. Siegwart, and M. Hutter, "The two-state implicit filter recursive estimation for mobile robots," *IEEE Robotics and Automation Letters*, vol. 3, no. 1, pp. 573–580, 2017.
- [67] M. Ramezani, Y. Wang, M. Camurri, D. Wisth, M. Mattamala, and M. Fallon, "The newer college dataset: Handheld lidar, inertial and vision with ground truth," in *2020 IEEE/RSJ International Conference on Intelligent Robots and Systems (IROS)*, 2020, pp. 4353–4360.
- [68] J. Sturm, N. Engelhard, F. Endres, W. Burgard, and D. Cremers, "A benchmark for the evaluation of rgb-d slam systems," in *2012 IEEE/RSJ international conference on intelligent robots and systems*. IEEE, 2012, pp. 573–580.
- [69] J. Nubert, S. Khattak, and M. Hutter, "Graph-based multi-sensor fusion for consistent localization of autonomous construction robots," in *2022 International Conference on Robotics and Automation (ICRA)*, 2022, pp. 10 048–10 054.



Turcan Tuna is a scientific researcher in the Robotic Systems Lab at ETH Zurich. He received his M.Sc. in Robotics, Systems & Control in 2022 from ETH Zurich. Previously, he completed a double major, B.Sc in Mechanical Engineering and Control & Automation Engineering, at Istanbul Technical University. He graduated from both of his B.Sc majors with distinction. His research interests include developing and deploying robust localization, perception, and mapping frameworks on robotic systems.



Julian Nubert is PhD student in the Robotic Systems Lab at ETH Zurich. He received his M.Sc. in Robotics, Systems & Control in 2020 from ETH Zurich. He is also affiliated with the Max Planck Institute through the MPI ETH Center for Learning Systems. His research interests lie in the field of robust robot perception, and how it can be used for the deployment of mobile robotic systems. Julian received the ETH silver medal and was awarded the Willi-Studer-Price for his accomplishments during his master studies.



Yoshua Nava is a Perception Software Engineer at ANYbotics AG (Zurich, Switzerland), where he specializes in point cloud-based localization and mapping. He received his masters degree in Systems, Control and Robotics from KTH Royal Institute of Technology (Stockholm, Sweden), and his bachelor's degree from Universidad Católica Andrés Bello (Caracas, Venezuela). His research interests broadly cover localization and mapping as a core skill for robot mobility, and as a way to increase situational awareness for robots and human operators.



Shehryar Khattak is a Robotics Technologist at the NASA - Jet Propulsion Lab. Previously, he was a post-doctoral researcher at the Robotics Systems Lab at ETH Zurich and the perception lead of team CERBERUS, which won the DARPA SubT Challenge (2021). He received his Ph.D. (2019) and MS (2017) in Computer Science from the University of Nevada, Reno. He also holds an MS in Aerospace Engineering from KAIST (2012) and a BS in Mechanical Engineering from GIKI (2009). His research focuses on developing perception algorithms to support real-time localization and mapping for field robotics applications.



Marco Hutter is Associate Professor for Robotic Systems at ETH Zurich. He received his M.Sc. and PhD from ETH Zurich in 2009 and 2013 in the field of design, actuation, and control of legged robots. His research interests are in the development of novel machines and actuation concepts together with the underlying control, planning, and machine learning algorithms for locomotion and manipulation. Marco is the recipient of an ERC Starting Grant, PI of the NCCRs robotics and digital fabrication, PI in various EU projects and international challenges, a co-founder of several ETH Startups such as ANYbotics AG.